8-2023

Chemostratigraphic and Paleoclimatic Studies of Cloverly Formation, Northern Wyoming, U.S.A

Queen Amarachi Kalu
University of Arkansas-Fayetteville

Chemostratigraphic and Paleoclimatic Studies of Cloverly Formation, Northern Wyoming, U.S.A

A thesis submitted in partial fulfillment
of the requirements for the degree of
Master of Science in Geology

by

Queen Kalu
Federal University of Technology Owerri
Bachelor of Technology in Geology, 2018

August 2023
University of Arkansas

This thesis is approved for recommendation to the Graduate Council.

_____
Celina Suarez, Ph.D.
Thesis Director

_____
Glenn Sharman, Ph.D.
Committee Member

_____
Phillip D. Hays, Ph.D.
Committee Member

Abstract

The Early – Late Cretaceous transition in Western North America recorded a period of rapid climatic and tectonic change in Earth's history. Major climate events associated with large igneous province eruptions caused several instances of ocean anoxic events (OAE) and perturbations to the global carbon (C) – cycle. These perturbations to the global C-cycle are observed in the bulk organic C record of both marine and terrestrial deposits and can be used to correlate units across major depositional basins. Major efforts are being made to generate time-constrained palaeontologic and paleoclimate information from the North American Cordilleran foreland basin and C-isotope chemostratigraphy can aid in making these correlations. This study uses the isotopic composition of bulk organic carbon from the Lower Cretaceous Cloverly Formation to constrain the age of the Cloverly Formation within the Bighorn Basin, Wyoming. The study also investigates paleoclimate proxies such as mean annual precipitation and atmospheric CO_2 concentrations. C-isotope chemostratigraphy of bulk organic carbon results range between -21‰ and -30.1‰ and average at -23.97 ‰. Two pedogenic carbonates nodules from the Little Sheep Member (CCC-12 and CCC-24) were analyzed for $\delta^{13}C_{org}$, $\delta^{13}C_{carb}$, and $\delta^{18}O_{carb}$. The Little Sheep Mudstone Member carbonate nodules have average $\delta^{13}C_{carb}$ values of -6.72 ‰ at CCC-12 and -7.25 ‰ at CCC-24. The mudstone organic C isotopic values of the carbonate nodules are -26.27 ‰ for CCC-12, and -25.9 ‰ for CCC-24. The S(z) values (soil CO_2 concentration) were estimated to be between 1000 – 3000 ppm, typical of micro-high vertic soils. Atmospheric pCO_2 concentrations are calculated using the paleosol CO_2 paleobarometer of Ekart et al. (1999) and are reported at S(z) = 2000 ± 1000 ppm. Atmospheric C-isotopic composition of pCO_2 is estimated using the $\delta^{13}C$ of bulk organic C in mudstones and the relationship between plant matter and pCO_2 outlined in Arens et al. (2000). Atmospheric pCO_2

values at 4 m above the Pryor Conglomerate, 14.5 m above the Cloverly-Morrison lithologic boundary are 352 ± 176 ppm and increase to 931 ± 465 ppm at 18.5 m. Mean annual precipitation (MAP) was calculated from weathering indices of metal oxides in soils using CALMAG and CIA-K equations. MAP increases up section from a minimum of 697- 984 mm/yr in the LSM to a maximum of 1291-1705 mm/yr in the Upper Himes Member. Given the maximum depositional age of the base of the Little Sheep Mudstone Member (129.4 ± 3.4 Ma) from D'Emic et al. (2019), a maximum depositional age for the lower Himes Member at Crooked Creek of 103.6 ± 1.3 Ma (D'Emic et al., 2019), the maximum depositional age of 112.09 ± 0.34 Ma (Carrano et al., 2021) from other Little Sheep Mudstone outcrops, and the high resolution C-isotope chemostratigraphic trend of the Crooked Creek Section (this study) constrains the positive C-isotope trend and decreasing (negative CIE) trend to the C-10 to C-11 C-isotope excursions associated with the CIE of Bralower et al. (1999) that occurs in the Late Aptian to Early Albian.

Acknowledgements

I would like to thank my advisor Dr. Celina Suarez, for giving me the opportunity to study in the United States. I appreciate her support, invaluable guidance, and resources that shaped and directed the success of my research. I am grateful to my committee members, Dr. Glenn Sharman, and Dr. Philip Hays, for giving me a strong foundation in sedimentary petrology and stable isotope geochemistry and for reviewing my thesis.

I thank the Cloverly Formation field work team including Dr. Glenn Sharman, Jack Fekete, Dr. Marina Suarez and her field crew, and Dr. Pete Makovicky and his field crew for their support throughout the field sample collection in northern Wyoming.

This research would not have been completed without the help of Lindsey Conaway and Erik Pollock at the University of Arkansas Stable Isotope Laboratory who helped with the analysis of my samples.

I appreciate the faculty and staff of the Department of Geosciences at the University of Arkansas for fostering an intellectually stimulating environment and providing access to necessary resources.

I extend my appreciation to the Suarez research group for their assistance. Worthy of mention is Clayton Forster, who provided immense assistance towards the completion of my thesis.

I also thank the geochemistry, stratigraphy, and paleoclimate geoscience community whose research works contributed greatly to my thesis and have inspired me to delve deeper into this area of research.

Finally, I am grateful to my parents, siblings, and in-laws for their unwavering support, understanding and encouragement. Their belief in my abilities has been the driving force towards my career.

Table of Contents

List of Figures

Chapter 1

Chapter 2

List of Tables

Chapter 1

Chapter 2

Chapter 1:

Introduction

Thesis Structure

This thesis has two chapters. Chapter 1 is a general introduction to the Early Cretaceous Period, carbon(C) isotope chemostratigraphy, the Cloverly Formation, and paleoclimate proxies used in the study**.** Chapter 2 is formatted as a manuscript that will be submitted for publication in Cretaceous Research. This chapter: "C-Isotope Chemostratigraphy and pCO_2 calculations from the Cloverly Formation in Northern Wyoming" includes details of the paleoclimate proxies used in the study, discussions/interpretations, and conclusion.

The Early Cretaceous Paleoclimate

The Early – Late Cretaceous Period is generally thought of a greenhouse climate that induced periods of ocean anoxic events (OAEs) but also saw periods of coolhouse events that occurred during the latest Aptian to Early Albian stages (Bodin et al., 2015; Erba et al., 2015; Lee et al., 2019; McAnena et al., 2013). Major geologic events such as the Sevier Orogenic event, continued sea-level rise of the Zuni Sequence, development of the Western Interior Seaway, continued rifting and break-up of Gondwanaland, global sea-level fall (North America Bering land bridge), and large igneous province (LIPs) eruptions greatly impacted the Cretaceous (Erba et al., 2015; Ernst & Youbi, 2017; Shurr et al., 1989; Suarez et al., 2017; Wignall, 2001). Large igneous province eruptions including the Paraná-Etendeka LIP (South America and Africa rifting), Ontong Java LIP, Kerguelen LIP, Caribbean-Columbian, Madagascar LIP, and Deccan Basalt traps (India) (Figure 1) resulted in several ocean anoxic events (e.g the Selli event (OAE1a), increased atmospheric CO_2 concentrations, increased

productivity, accelerated hydrologic cycles recorded in O-isotope records and marine extinctions (Erba et al., 2015; Ernst & Youbi, 2017; Wignall, 2005). Life events that occurred during the Cretaceous including major expansion of single celled organisms such as foraminifera and coccolithophores; continued evolution of ammonites into large forms; diversification of marine reptiles (mosasaurs and plesiosaurs), reef-forming clam populations (Rudist bivalves) and Scleractinian corals; terrestrial evolution such as continued diversification of dinosaur, evolution of angiosperms, evolution of pollenating insects, and expansion of birds and mammals (Grimaldi, 1999; Harrell Jr et al., 2016; Lloyd et al., 2008; Martin, 2002).

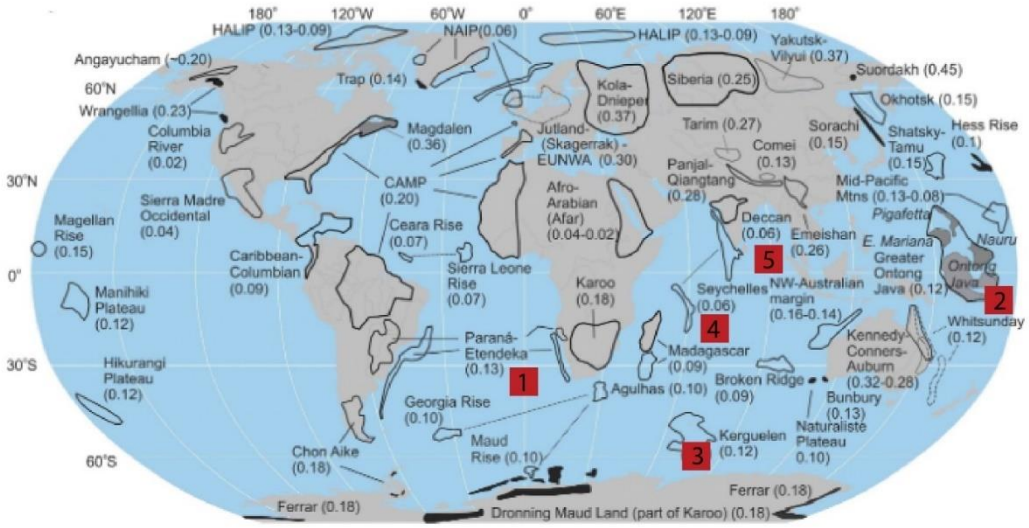

Figure 1: Large igneous provinces (red squares) that erupted during the Cretaceous Period. 1. Parana Etendeka LIP 2. Ontong Java LIP 3. Kerguelen 4. Madagascar, 5. Deccan traps. Modified slightly from Ernst & Youbi (2017)

Table 1: Large igneous province eruptions and associated events. Modified from Wignall (2005)							
Large igneous province	Global warming	Ocean anoxia	Methane release from gas hydrates	Ocean calcification crisis	Significant extinction events	~Age	Age source
Deccan Traps	yes	moderate	no	moderate	End – Cretaceous (K/T)	66 Ma	(Schoene et al., 2015)
Caribbean-Columbian, Madagascar	yes	End-Cenomanian Stage	no	no	yes	90 Ma	(Cucciniello et al., 2010)
Kerguelen Plateau	cooling	no	no	yes	moderate	119-110 Ma	(Coffin, 2002; Frey et al., 2003)
Ontong Java	yes	Early Aptian Stage OAE 1a	moderate	yes	no	124 - 120 Ma	(Bond & Wignall, 2014; Timm et al., 2011)
Parana-Etendeka	no	Valanginian Stage	no	yes	no	133 Ma	(Almeida et al., 2018; Florisbal et al., 2014)

The Carbon Cycle and Carbon Isotope Chemostratigraphy

Degassed carbon from the Earth's interior passes through the exogenic system (atmosphere, terrestrial biosphere, surface ocean, intermediate and deep ocean, and reactive marine sediment), and influences the climate prior to burial as carbonates or organic carbon (Lee et al., 2019; Figure 2, Figure 3). Carbon cycling in the atmosphere and ocean reservoirs occur over short time scales of ~ <1000 years (Lee et al., 2019) (Figure 3). The deep-C reservoir is connected to the surface reservoir via volcanism and metasomatism. Within the surface reservoir,

are a number of smaller reservoirs such as the ocean, atmosphere, biosphere, and lithosphere. Changes in the flux of one carbon reservoir to another results in perturbations in the global C-cycle and the isotopic compositions of these reservoirs can be used to correlate units across major depositional basins through records in bulk organic C- isotope record of both marine and terrestrial deposits (Foreman et al., 2012; Herrle et al., 2015; Ludvigson et al., 2015; Suarez et al., 2017; Suarez et al., 2013; Wignall, 2001).

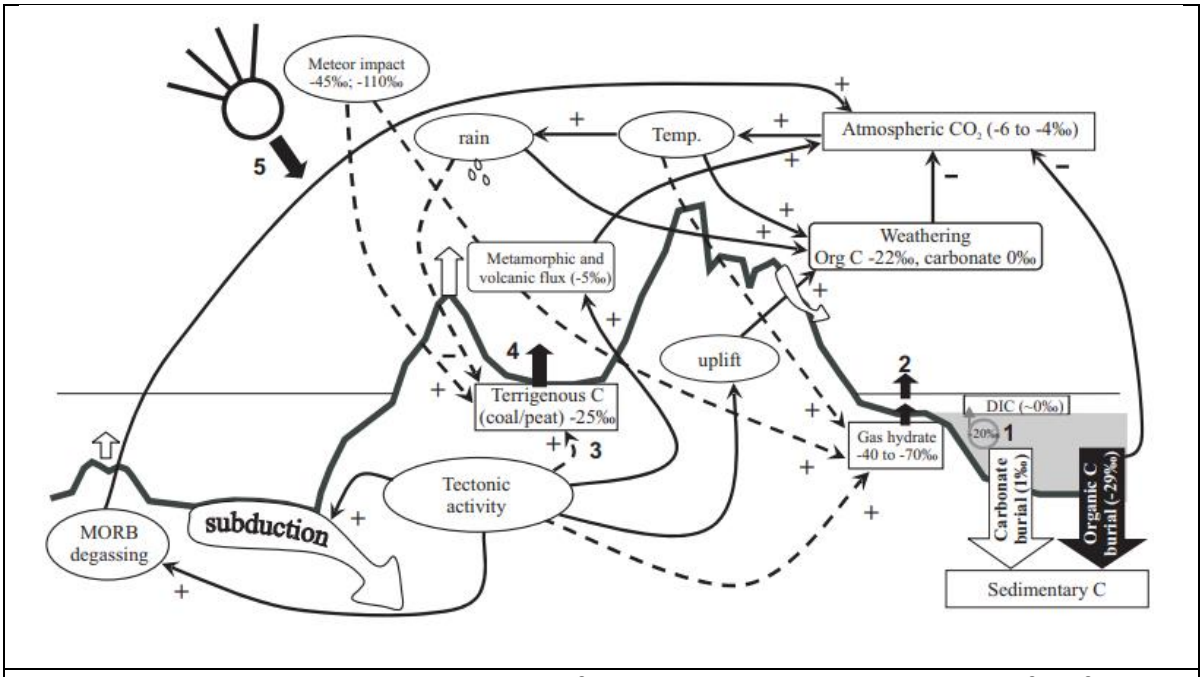

Figure 2: Long term carbon cycle adapted from Breugel (2006), *initially modified from* Kump & Arthur (1999)

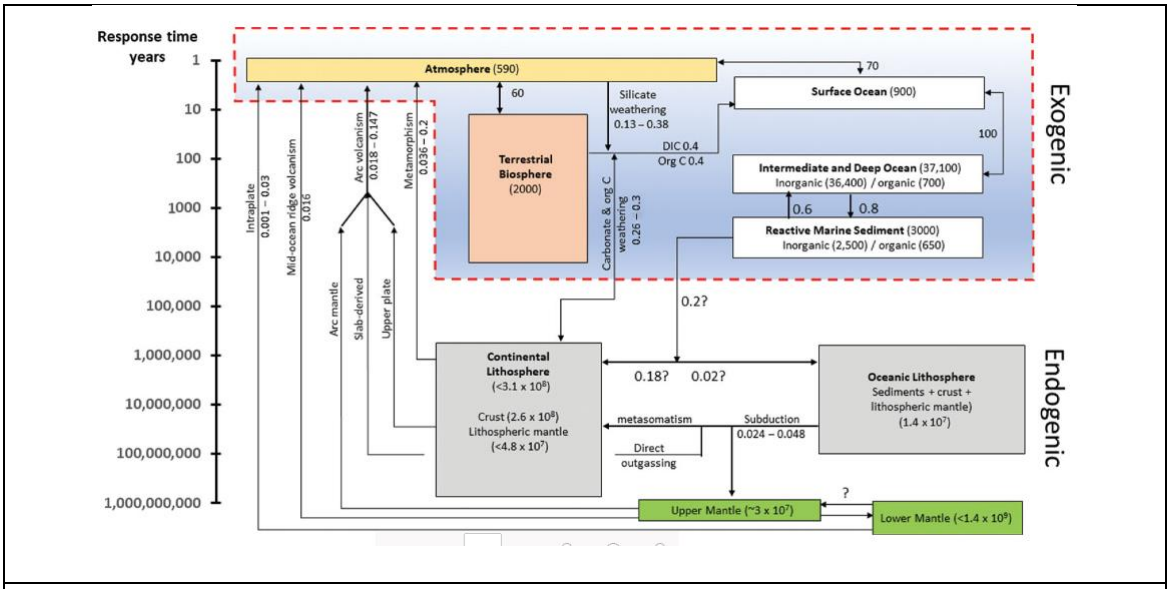

Figure 3: Endogenic and exogenic carbon cycle processes with reservoirs placed according to the estimated residence time (in years) assuming a steady state system. Adapted from Lee et al. (2019)

Perturbations within the carbon cycle are seen in carbon isotope chemostratigraphy as negative and positive excursions. A complex interaction of the biosphere, lithosphere, and atmosphere can affect the magnitude of these excursions as well as whether a positive or negative response occurs in the carbon isotope system. In general, an increase in the amount of atmospheric CO_2 (depending on the source of CO_2 and it's isotopic composition) can cause increased silicate weathering to the oceans, increased primary productivity, increased rates of burial of organic matter, and dissolved inorganic carbon (DIC) in oceans, which results in a positive carbon isotope excursion (PCIE) (Arthur et al., 1988; Wignall, 2001, 2005). The increase in primary productivity and burial of organic matter sequesters light carbon since photosynthetic fractionation causes sequestering of ^{12}C from the DIC pool, resulting in a positive C-isotope excursion. This is in part due to photosynthetic fractionation of C-isotopes. Photosynthetic organisms (such as plants) take up carbon dioxide during photosynthesis and

convert it to sugar through two pathways: the Calvin Cycle (C_3 plants) and the Hatch -Slack Cycle (C_4 plants). Carbon fixation with ribulose -1, 5-biphosphate (RuBP) carboxylation (C_3 pathway) are used by C_3 plants. The total fractionation for C_3 plants falls within the range of -20 to -30 as determined from bacterial and RuBP carboxylation but may be up to -34 ‰ for terrestrial plants (White, 2014). C_4 plants which occurred only after evolution of C_4 grasses in the Miocene Epoch use phosphoenolpyruvate carboxylase to form oxaloacetate (Sundquist & Visser, 2003; White, 2014) that results in a less fractionation and thus more enriched $\delta^{13}C$ values (-9 to -17 ‰) (Ballentine et al., 1998). Due to this decreased fractionation, C-isotope chemostratigraphy can only be related to global CO_2 prior to C_4 plant evolution using C_3-dominated systems. Thus, kinetic fractionation of isotopically light to heavy carbon ($^{13}C/^{12}C$), ^{12}C is incorporated into plants leaving the atmosphere enriched in ^{13}C (Saltzman & Thomas, 2012; White, 2014)

Negative C-isotope excursions (NCIEs) are more difficult to explain, but most instances of NCIEs are related to large igneous provinces in which a pool of volcanic isotopically light C is volatilized into the atmosphere (Hoefs 2009; Breugel, 2006; Grocke, 2002; Hesselbo et al., 2000; Jahren et al., 2001; Kump & Arthur, 1999; McInerney & Wing, 2011; Röhl et al., 2007; Zeebe et al., 2009). This can include volatilization of C-isotopically light methane (CH_4) hydrates as ocean temperatures increase (greenhouse warming) and volatilization of organic-rich sediments (Breugel, 2006; Wignall, 2005). In these instances of large igneous province eruptions, a typical pattern observed in the C-isotopic record is an initial NCIE as light C sources are volatilized, followed by a PCIE as primary productivity in enhanced, and then a stabilization to pre-excursion $\delta^{13}C$ values. Thus, the pattern of positive and negative CIEs can be used to explain the multi-faceted mechanisms of climate change brought on by volcanic activity (Bond

& Wignall, 2014; Breugel, 2006; Cramer & Jarvis, 2020; Harper et al., 2020; Röhl et al., 2007; Zachos et al., 2005).

The Cloverly Formation and Paleoclimate Proxies Used in the Study

The Cloverly Formation comprises the Pryor Conglomerate, the Little Sheep Mudstone Member, and the Himes Member (Lower and Upper Himes Members) which were previously classified by Ostrom (1970) as Units IV, V, VI, and VII respectively. This research focuses on outcrops from the Cloverly Formation and the overlying Sykes Mountain Formation located in the Crooked Creek area, Big Horn Basin, northern Wyoming. In the study area, the basal member – the Pryor Conglomerate (PC) overlies the Jurassic Morrison Formation with a disconformable contact, the Little Sheep Mudstone (LSM) Member overlies the Pryor Conglomerate, and the overlying Himes Member has disconformable contact with the LSM Member. There is a gradual and transitional contact between the upper Himes Member and the overlying Sykes Mountain Formation in which an increase in organic matter and proximal coastal facies occurs D'Emic et al. (2019); Figure 4).

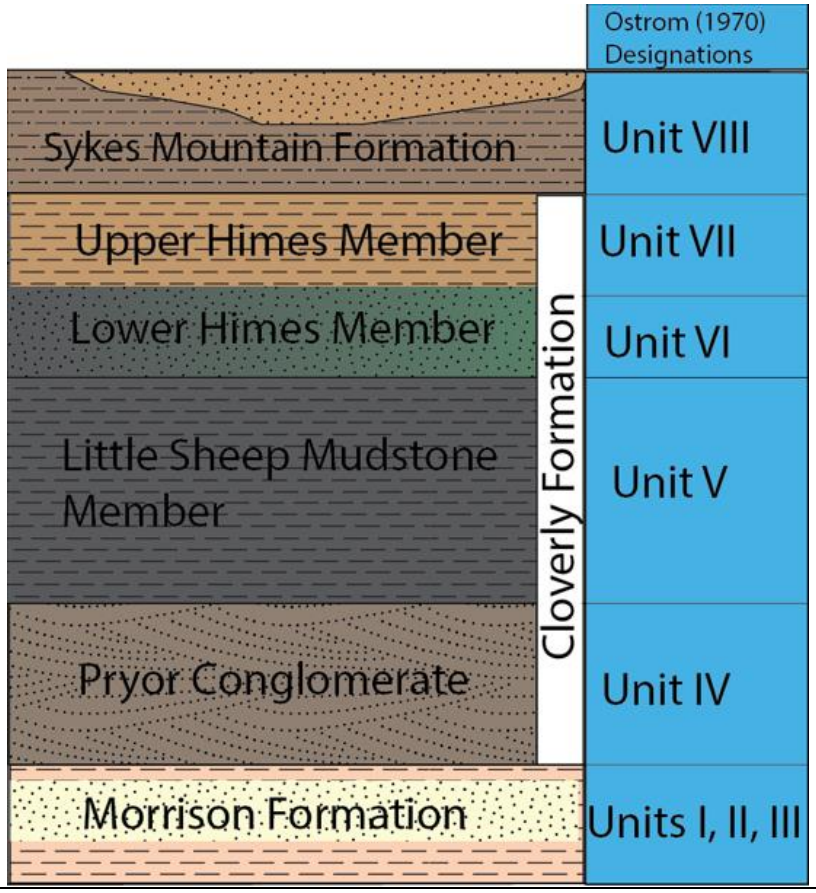

Figure 4: General stratigraphy of the Cloverly Formation.

The purpose of this study is to 1) constrain the age of the Cloverly Formation as well as important vertebrate fossil localities within the formation and 2) generate climate proxy data from the Cloverly Formation.

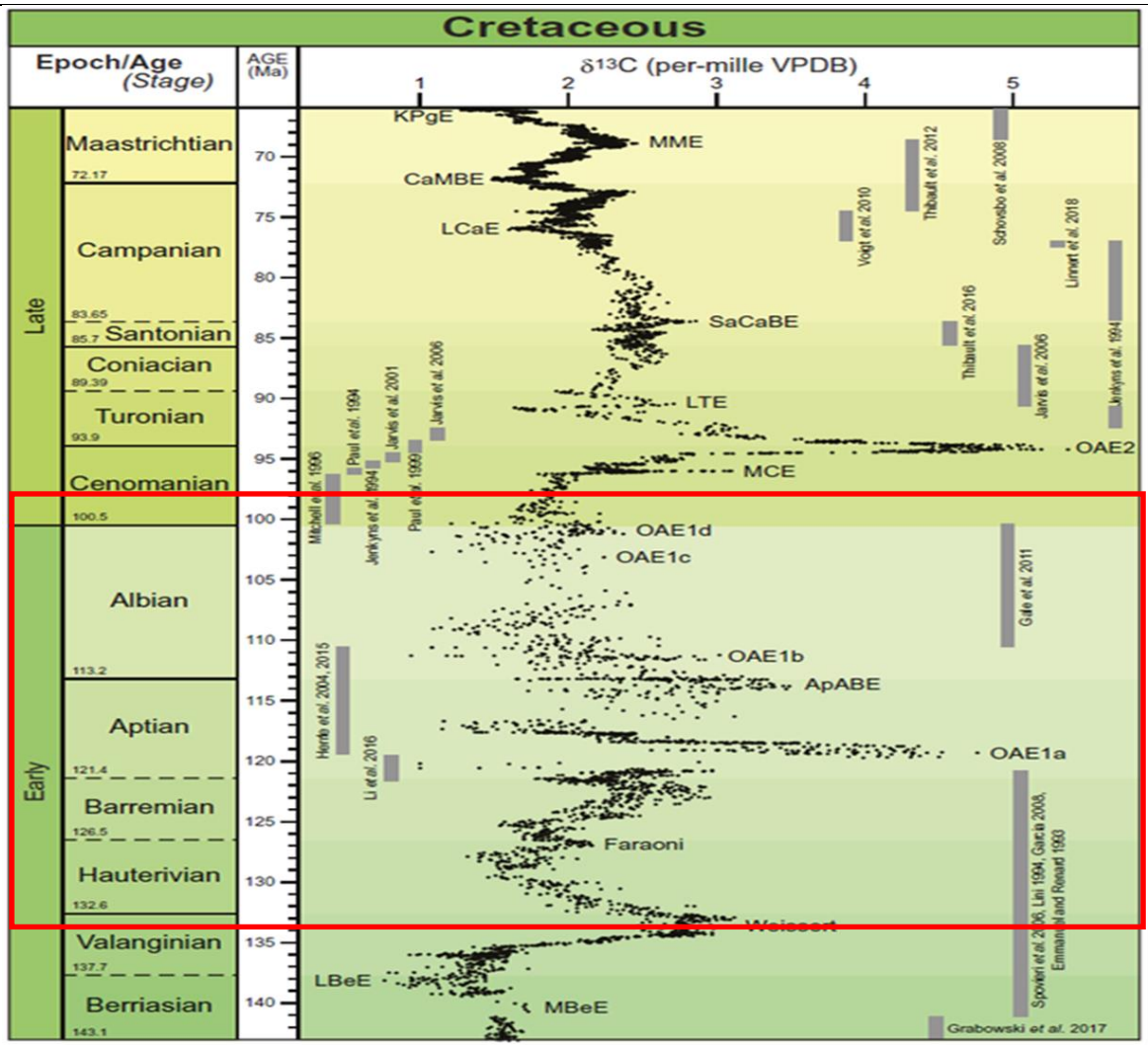

Figure 5: Variation in $\delta^{13}C_{carb}$ through the Cretaceous by Cramer & Jarvis (2020)

To do this (Chapter 2), we generate bulk organic ($\delta^{13}C_{org}$) chemostratigraphic data from 164 samples, and $\delta^{13}C_{carb}$, and $\delta^{18}O_{carb}$ values from two pedogenic carbonate samples with the goal of calculating atmospheric pCO_2 and calculate mean annual precipitation (MAP) from weight percent metal oxides in 13 vertic soils exhibiting pedogenic features. The chemostratigraphic curve from this study was correlated to age constrained C-isotope chemostratigraphic records from marine carbonates (such as Herrle et al. (2015). This correlation is constrained by ages determined from previous studies (D'Emic et al., 2019) of detrital zircon U-Pb geochronology

with laser ablation inductively coupled plasma mass spectrometry (LA-ICPMS) and chemical abrasion isotope dilution thermal ionization mass spectrometry (CA-ID-TIMS) from the Crooked Creek section, and by the age of the Little Sheep Mudstone Member from volcanolithic units of the Little Sheep Member in other outcrops of the Cloverly Formation (Carrano et al., 2021).

Chapter 2

C-Isotope Chemostratigraphy and pCO_2 calculations from the Cloverly Formation in Northern Wyoming

Abstract

The Early – Late Cretaceous transition in Western North America recorded a period of rapid climatic and tectonic change in Earth's history. Major climate events associated with large igneous province eruptions caused several instances of ocean anoxic events and perturbations to the global carbon (C) cycle, resulting in rises in pCO_2, global warming, and rising sea-level culminating in the formation of the Western Interior Seaway (WIS). Major efforts are being made to generate paleoclimate information from the Cordilleran foreland basin, but the lack of time-constrained palaeontologic and paleoclimatic data makes correlation of global carbon (C)-cycle perturbations to the Early – Late Cretaceous biotic transition in Western North America uncertain. Here, we apply C-isotope chemostratigraphy to determine the extent to which the Cloverly Formation of Wyoming captures paleoclimate change. We also analyzed pedogenic carbonates from two horizons. These two samples were thin sectioned to observe calcite microfabrics. Micro-sampling of the facing billets of these carbonates and analysis of $\delta^{18}O_{carb}$ and $\delta^{13}C_{carb}$ were conducted to examine the diagenetic history of the pedogenic carbonate nodules with the goal of calculating paleo-CO_2 concentrations. Finally, we collected major elemental oxide concentrations from X-ray fluorescence analysis of interpreted paleosol B-horizons to calculate mean annual precipitation. The constructed high-resolution C-isotope chemostratigraphic record reveals an average $\delta^{13}C$ value of -23.97‰. A positive C-isotope excursion occurs between 15m and 34m with a broad positive C-isotope excursion of -21 ± 0.71 ‰ at 15 m in the lower LSM Member. This excursion was correlated to positive $\delta^{13}C_{carbonate}$

chemostratigraphic curve of Herrle et al., (2015), and given known detrital zircon ages, we correlate the broad positive CIE as the C-9 to C-11 segments of Bralower et al. (1999) that occurs in the Late Aptian to Early Albian. Atmospheric pCO_2 concentrations are calculated using the paleosol CO_2 paleobarometer of Ekart et al. (1999) and are reported at S(z) = 2000 ppm with an uncertainty of 1000 ppm. Atmospheric C-isotopic composition of pCO_2 is estimated using the $\delta^{13}C$ of bulk organic C in mudstones and the relationship between plant matter and pCO_2 outlined in Arens et al. (2000). Atmospheric pCO_2 values at 14.5m above the Morrison Formation 352 ± 176 ppm and increase to 931 ± 465 ppm at 18.5 m. Finally, the MAP gradually increases up section from a minimum of 697mm/yr to 984 mm/yr at 17.75m within the Little Sheep Mudstone to 1291mm/yr to 1705 mm/yr at 55.05m in the upper Himes Member. The correlated high resolution chemostratigraphic positive excursion with age constraints from Carrano et al. (2021); D'Emic et al. (2019), places the Little Sheep Mudstone Member within the Late Aptian to Albian Stage. The lower pCO_2 values relative to the rest of the Cretaceous and the correlation with the C-9 to C-11 CIE are consistent with periods of cooling associated with the emplacement of the Kerguelen LIP. Renewed warming following this "cold snap" in the Early Albian is consistent with the increasing MAP.

Introduction

The Cretaceous Period has historically been interpreted as a "hot-house" or "warm-house" climate due to its overall higher CO_2 concentration in the atmosphere. However, as high-resolution climate records come to light, subtle complexities such as "cold" or "cool-snaps" are known to have occurred throughout the Cretaceous (Bodin et al., 2015; McAnena et al., 2013). This complex interaction of the Cretaceous Earth system is preserved in the stratigraphy of sedimentary rocks deposited within the Western Interior Foreland Basin. The Sevier Fold and Thrust Belt resulted in a major change in the depositional setting of North America during the Cretaceous and superimposed on this was a rise in sea-level that caused the ancient Boreal Sea and the ancient Gulf of Mexico to connect, creating an epicontinental sea known as the Western Interior Seaway (WIS). This caused the deposition of non-marine sediments in the Cordilleran foreland basin to the west of the WIS including the Cloverly Formations in northern Wyoming (DeCelles & Burden, 1992).

The Cretaceous Period also recorded higher concentrations of atmospheric CO_2 which contributed to higher temperature, productivity, and biotic distribution, although details of these connection are not fully understood (Arens & Jahren, 2000; Cramer & Jarvis, 2020; Ekart et al., 1999). These C-isotope perturbations during the Cretaceous are also associated with large igneous province eruptions (LIP) as well as the >1,100 km Cordillera that extended from Canada to South America (Price 1986) and caused several instances of ocean anoxic events (OAEs) and perturbations to the global carbon (C) – cycle. These C-isotope records can be used to generate time-constrained paleontologic and paleoclimate information from the Cordilleran foreland basin (D'Emic et al., 2019; Ludvigson et al., 2015; Suarez et al., 2013).

This study aims at investigating the Cretaceous C-isotope and climate record for the northernly WIB recorded by the Cloverly Formation of the Big Horn Basin, Wyoming. The Cloverly Formation may have spanned the Valanginian to Cenomanian stages (ca. 140 – 98 Ma) (D'Emic et al., 2019), however a recent study by Carrano et al. (2021) dated a volcanolithic unit within the lower Little Sheep Member that directly overlies the basal Pryor Conglomerate as 112.9 ± 0.34 Ma, suggesting an Early Albian stage for the oldest fossil-bearing units of the Cloverly Formation. By determining the organic carbon isotopic record of the Cloverly Formation that is constrained by recent geochronologic studies, more accurate age-constraints can be determined for the Cloverly Formation. In this study, the C-isotope record is augmented by paleoclimate proxy data. Pedogenic carbonates are used to calculate atmospheric pCO_2 concentrations and weight percent metal oxides are used to calculate mean annual precipitation.

Geologic Setting

Lower Cretaceous rocks are exposed throughout Wyoming along the flanks of Laramide basement block uplifts at the front of the Sevier fold and thrust belt (DeCelles & Burden, 1992; Elliott et al., 2007). The Cloverly Formation consist of sediments derived from braided and meandering rivers, thick flood plain derived paleosols, evaporitic lacustrine deposits, and in the upper part of the formation, organic rich coastal plain deposits (DeCelles, 2004; DeCelles & Burden, 1992; D'Emic et al., 2019; Moberly, 1960; Ostrom, 1970). In the Bighorn Basin, the Cloverly Formation is divided into three basic lithostratigraphic units: the Pryor Conglomerate, the Little Sheep Mudstone Member, and the Himes Member (Moberly, 1960)

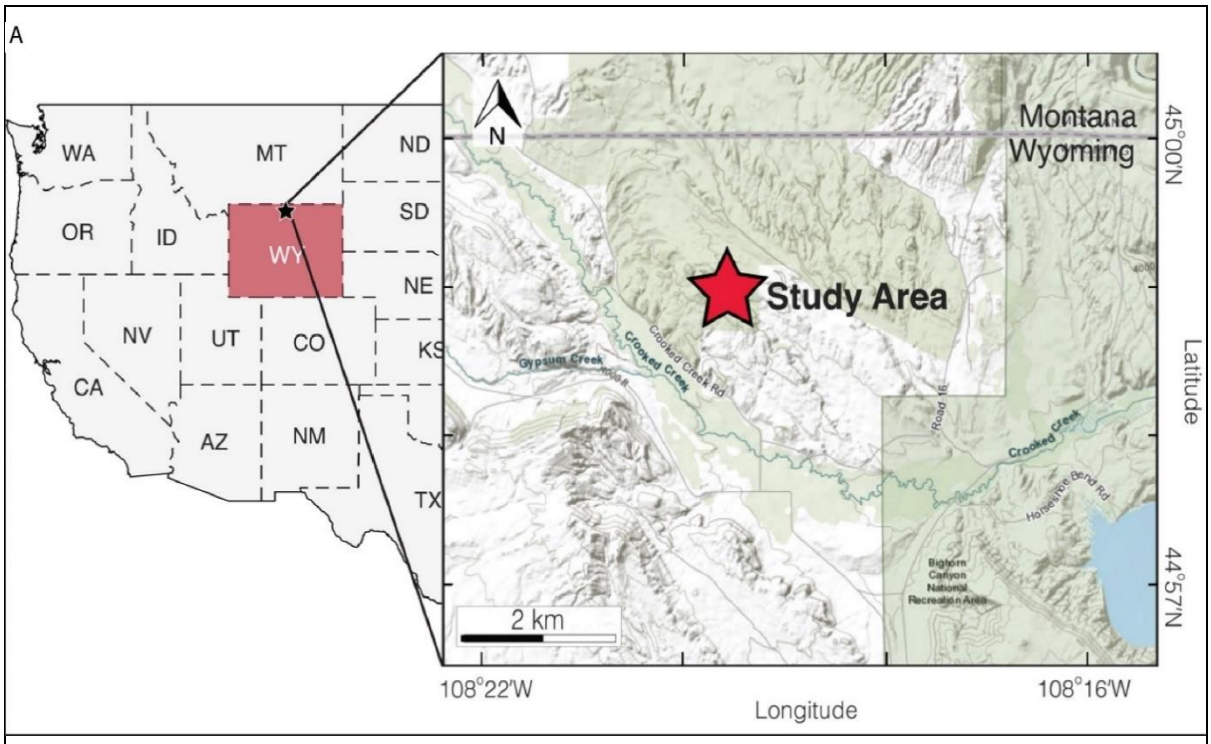

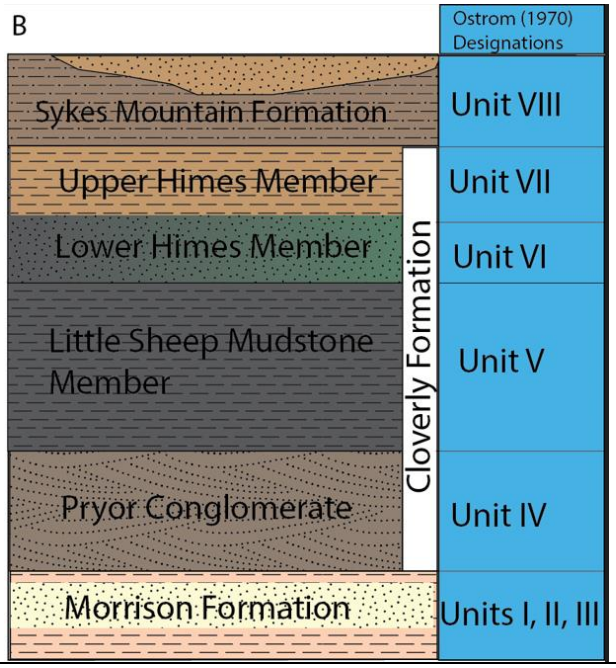

Figure. 1: Study area (A) of the Crooked Creek sections and generalized stratigraphy (B)of the Cloverly Formation in the Bighorn Basin with Ostrom (1970) *designations.*

As the Boreal Sea transgressed from the north to eventually merge with the ancestral Gulf of Mexico and form the Western Interior Seaway, the Sykes Mountain Formation began nearshore deposition and conformably overlies the Cloverly Formation (Figure 1).

Pryor Conglomerate

The Pryor Conglomerate is the lowest member of the Cloverly Formation (Moberly, 1960; Ostrom, 1970). It was most likely deposited ca. 140 – 130 Ma in response to the initiation of the Sevier Orogeny shedding sediments from the west to the east and from the south to the north-northeast (DeCelles & Burden, 1992; D'Emic et al., 2019; Ostrom, 1970). Deposition was through a shallow, transient, gravel-bed braided stream system (DeCelles & Burden, 1992). It preserves well–defined massive and horizontally bedded basal chert pebble and quartzite-clast conglomerate as well as medium to fine cross-bedded sandstone (Moberly, 1960). The Pryor Conglomerate is an erosional lag deposit due to its underlying disconformity with the Morrison Formation (Oreska et al., 2013). The age range between ~140 Ma of the Pryor Conglomerate (D'Emic et al., 2019) and the youngest Morrison Formation from recalibrated $^{40}Ar/^{39}Ar$ Laser fusion age of ~150 Ma (Trujillo & Kowallis, 2015) in the Bighorn Basin indicates a lack of deposition of ca.10 Ma. The oldest age for the CF comes from this member.

Little Sheep Mudstone Member

The Little Sheep Mudstone Member (LSM) overlies the Pryor Conglomerate in some places but in others, directly overlies the Morrison Formation (D'Emic et al., 2019; Moberly, 1960). It is considered Unit V of Ostrom (1970) and comprises multi-colored bentonitic mudstones that are grey to dark grey in color, with occasional sandstone and limestone units (Ostrom, 1970). The LSM consists of clay composed of montmorillonite, illite, kaolinite and smectite, indicative

of the weathering process of volcanic ash with the middle portion of the LSM exhibiting an evaporative lake sequence (Moberly, 1960; Zaleha, 2006). D'Emic et al., (2019) described the middle portion of the LSM as an evaporative lake sequence based on the presence of gray to black organic rich bentonitic mudstone with interbedded nodular limestone, chalcedony, and gypsum deposits. D'Emic et al. (2019) reanalyzed published age ranges based on palynomorph biostratigraphic data from central and northern Wyoming (DeCelles & Burden, 1992; Furer, 1970) with ages spanning from 86 -145 Ma for the Little Sheep Mudstone Member. Analyses of detrital zircon grains from the Little Sheep Member yielded dates from the pre-Aptian to the Albian Stages. D'Emic et al. (2019) suggested the Little Sheep Mudstone Member was deposited during a period of low sediment supply ca. 124 – 109 Ma with dates specifically within 129.4 ± 3.4 Ma (LA-ICPMS) at the base of the Little Sheep Mudstone Member near Shell, Wyoming on the eastern side of the outcrop belt, 124.06 ± 0.12 Mya (CA-ID-TIMS) in the middle of the Little Sheep Mudstone Member on the north side of Cody, WY and 109.09 ± 1.1 Ma (LA-ICPMS) in the middle of Little Sheep Mudstone Member in the southwest side of Cody, WY (D'Emic et al., 2019). In contrast to the study by D'Emic et al. (2019), U/Pb geochronology of zircon reported by Carrano et al., (2021) suggest that a distinctive hard white unit that is presumably volcanolithic and often observed in the lower LSM in some localities places the LSM fully within the Albian, and reports age of 112.09 ± 0.34 Ma (CA-ID-TIMS). The depositional environment of the upper part of the Little Sheep Mudstone Member has been interpreted as alluvial to overbank soil sequences containing abundant vertebrate microfossil bonebeds including various dinosaurian remains such as *Deinonychus sp.*, *Tenontosaurus*, presence of gastrolith, various mammalians, chondrichthyians, osteichthyians, amphibians, and other archosaurs such as testudines (turtles), crocodilian, and squamates with some fauna persisting

into the Himes Member (D'Emic et al., 2019; Nudds et al., 2022; Oreska et al., 2013; Ostrom, 1970). Several palynological studies (e.g DeCelles & Burden, 1992; Furer, 1970; Knowlton, 1916; Nolan, 2000; Vuke-Foster, 1982; Wieland, 1905; Zaleha, 2006) have been conducted, but, ambiguous stratigraphic location of samples, misidentification, and insufficient documentation of specimens have resulted in age-designations ranging between Berriasian to Albian (D'Emic et al., 2019).

The Little Sheep Member is most notable for its paleoflora preserved within its lacustrine units. The presence of cycad *Nilsonia nigracollensis,* a plant macro fossil is suggestive of an earliest Cretaceous age based on its co-occurrence in the Lower Cretaceous Lakota Formation of South Dakota (Wieland, 1905). Some Mesozoic conifer shoots and fern leaves such as the conifer *Coniopteris hymenophylloides*, Dipteris sp., and *Microphyopteris sp.* are also preserved. Also found in the Little Sheep Member include gingkoes as well as the *bennettitalean Zamites* sp. These floras are typical of pre-angiosperms flora, and it is important to note that no angiosperms have been found within the Little Sheep Member.

Himes Member

The Himes Member is the youngest member of the three members of the CF with MDA of 103.6 ± 1.3 Ma (LA-ICPMS age) at the base the Himes Member in Crooked Creek section, northern Wyoming (D'Emic et al., 2019). The Himes Member disconformably overlies the LSM and is separated into two informal units, the lower Himes, and the upper Himes units (Mantzios, 1986; Moberly, 1960; Ostrom, 1970; Ostrom, 1970). Himes sediments were primarily sourced from the east as deposition continued during the mid – late Albian to early Cenomanian ca. 109 to 98 Ma (D'Emic et al., 2019). The lower Himes Member is characterized by litharenite and quartz arenite sand bodies with unique lenticular geometries that overlap laterally in outcrop. The

conglomeratic portions contain clasts of quartzite, diagenetically altered limestone, and chert with trough cross bedding and ripple lamination (Moberly, 1960; Zaleha & Wiesemann, 2005). The deposits are interpreted as meandering river systems and floodplain environments (D'Emic et al., 2019; Moberly, 1960; Ostrom, 1970). The upper Himes Member (Unit VII of Ostrom (1970) consists of highly mottled and multi-colored red and green mudstones and siltstones with some pedogenic carbonate nodules. *Deinonychus sp*. and *Tenontosaurus sp*. persists into the middle Himes Member (Nudds et al., 2022; Ostrom, 1970). The upper part of the upper Himes member preserves a uniquely different flora from the Little Sheep Member. Some species of *Athrotaxis* such as seed cones of *Athrotaxites yumenensis* (Dong et al., 2014), the conifer *Athrotaxites berryi* (D'Emic et al.,2019), and most notably, a diverse angiosperm flora such as *Populus potomacensis, Sapindopsis sp.*, are well preserved in the upper Himes Member (D'Emic et al., 2019). The angiosperm flora suggests at the oldest a Barremian age, and more likely an Albian age for the Himes. Other notable vertebrate remains such as *Sauroposeidon.*,(D'Emic et al., 2019), and amphibian *Albanerpeton ektopisitikon,* sp.nov.,(Carrano et al., 2021) are also present.

Material and Methods:

Samples were collected at 25 cm intervals where possible near Crooked Creek, Bighorn Basin Northern Wyoming (Figure 2). Where present, carbonate nodules were collected and analyzed for both O and C-isotope analysis of preserved micrite. Samples were oven dried at 48 ℃ upon being returned from the field.

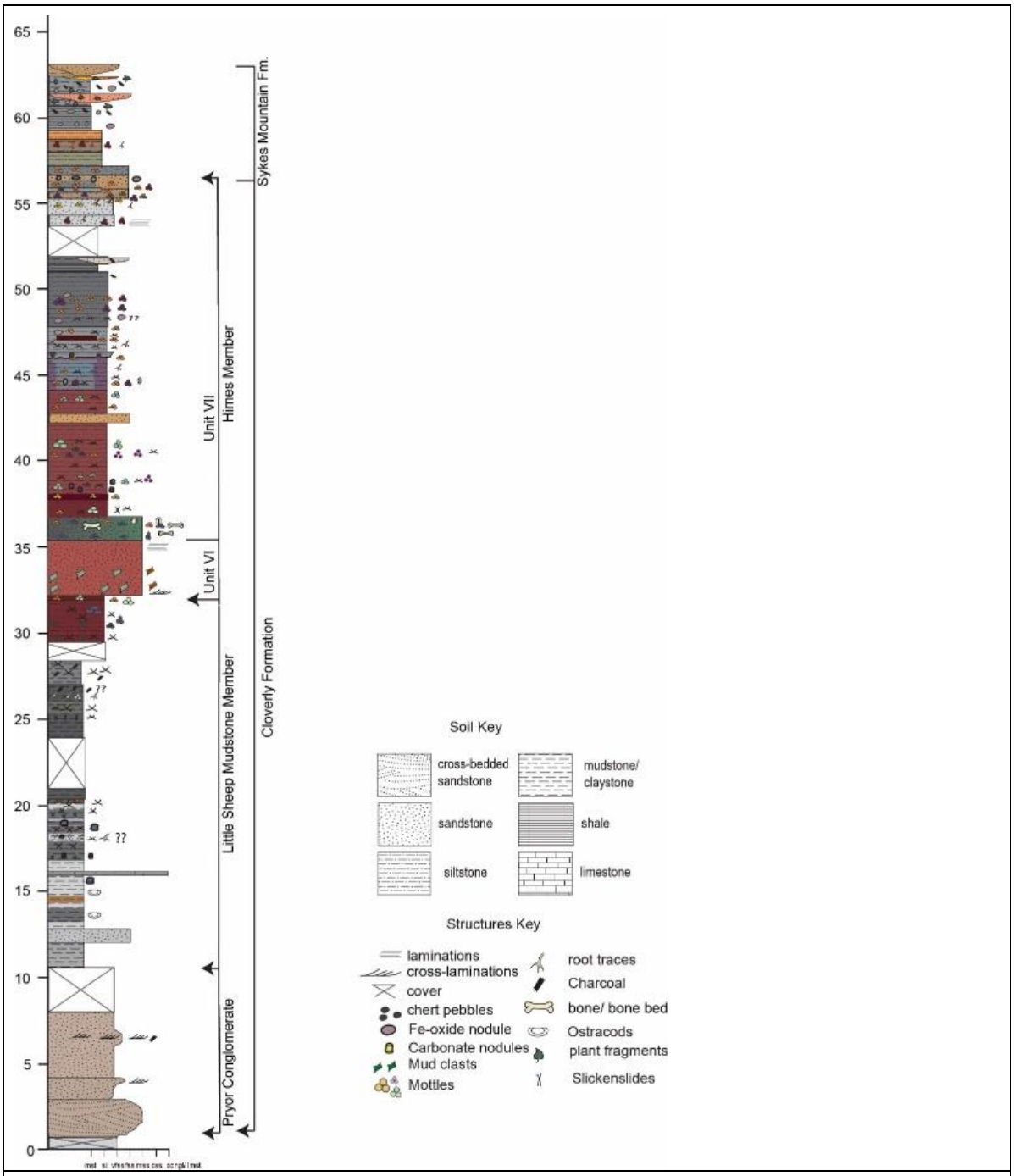

Figure 2: High resolution stratigraphic section of Cloverly Formation at Crooked Creek Section. Y-axis is in meters

Organic Carbon Isotope Analysis

The collected samples were prepared for C-isotopic analysis of bulk organic carbon. Using the method of Suarez et al. (2013). Samples were cleaned of modern organic material (roots) and crushed into a fine powder with a mortar and pestle and prepared for decarbonation. One gram of powder was decarbonated in 30 mL of 3M HCl. The samples were then reacted for two to four hours to ensure completion of the reaction. When the reaction reached completion, the samples were rinsed with deionized water until the sample was at a neutral pH. The samples were dried in an oven at 48°C and re-crushed into a fine powder. Samples were analyzed for bulk organic carbon isotopes via elemental analyzer (EA) Isolink coupled to a Delta V Plus isotope ratio mass spectrometer (IRMS) at the University of Arkansas Stable Isotope Laboratory (UASIL). Samples were reported in delta notation relative to Vienna Pee Dee Belemnite (VPDB). Calibration of organic carbon samples were relative to both internal and international isotope standards, this includes Sandy soil (−26.29 ± 0.2‰, material standard); Corn Maize (−11.32 ± 0.06‰, actual=−11.32‰, high standard); White River Trout (−26.63. ± 0.07‰, actual=−26.63‰, low standard), Benzoic acid (-27.77 ± 0.21, actual -27.64 ‰), and ANU Sucrose (−10.48 ± 0.148‰, actual=−10.45‰). Carbon isotope values were plotted relative to stratigraphic location for bulk organic C and the resultant data reported in delta notation.

Carbonate Petrography and Analysis

For this study, pedogenic carbonate nodules were sampled where present and logged into the measured section. The nodules were thin sectioned and micro-sampled for different carbonate phases (sparite versus micrite). Approximately 0.25-0.30 mg of powder was drilled and weighed into 4.5 mL Excetainer ® vials. Samples were reacted with 105% phosphoric acid at room temperature on a Gas Bench II. The produced CO_2 were analyzed on a Delta V

Advantage Mass Spectrometer. Calibration of carbonate samples was relative to NBS-19 (with a $\delta^{13}C$ average value of 1.95‰ ± 0.13 vs VPDB) and two in-house standards, UASIL 22 (with a $\delta^{13}C$ average value of -35.60‰ vs VPDB) and UASIL 23 (with a $\delta^{13}C$ average value of -0.60‰). The resultant data of carbon and oxygen isotope values were reported in delta notation relative to VPDB. A C-O-isotope cross plot (Figure 4) was created to examine the diagenetic history of the pedogenic carbonate nodules with the goal of calculating paleo-CO_2 concentrations.

Weight percent Metal Oxide Analysis

Identified B-horizons (units with clear slickensides, root traces, or accumulations of mineral, (e.g. pedogenic carbonates) were identified from stratigraphic section notes. B-horizon sediments were powdered and prepared for glass beads and pressed pellet analysis using X-Ray Fluorescence (XRF) spectrometry. Analysis was done at the University of Texas at San Antonio, Department of Geological Sciences. A total of 13 samples from across the section from the Little Sheep Mudstone Member and the Himes Member were analyzed. Samples were powdered and ~1.0 to 2.0 g of each sample were weighed into a crucible, weights recorded, and dried in the oven at 1050 ℃ for 90 minutes. The samples were reweighed after cooling and loss on ignition (LOI) was calculated. 0.001g of each dry sample was weighed and transferred into the glass mortar with lithium tetraborate, $Li_2B_4O_7$, and mixed for 30 seconds. The resulting mold was placed in a mold holder, the fusion program was selected, and fusion parameters monitored. Each sample was processed as a glass bead for major elements analysis.

Paleoclimate Proxy Calculations:

Soil elements such as Ca, Mg, Na, Al, and K are lost through weathering forming basic oxides such as CaO, MgO, Na_2O, and K_2O and become depleted with increasing rainfall relative to Al_2O_3. The variations in precipitation and temperature control chemical weathering in soils (Sheldon et al., 2002). Vertisols are clayey soils with shrink-swell properties, pedogenic characteristics, slickensides, and iron oxides (Lynn & Williams, 1992; Nordt & Driese, 2010; Sheldon et al., 2002). Nordt & Driese (2010) developed a relationship for vertisols; chemical weathering indices such as fluxes of magnesium and calcium (CALMAG), and Maynard (1992) developed the chemical index of alteration without potassium (CIA-K) equation.

Two weathering index parameters were calculated: 1) chemical index of alteration minus potassium (CIA-K) (Maynard, 1992)

$$CIA\text{-}K = Al_2O_3/ (Al_2O_3 + CaO + Na_2O) \times 100 \qquad \text{(Equation 1)}$$

and CALMAG using the equation of Nordt & Driese (2010):

$$CALMAG = 100(Al/Al + Ca + K + Na) \qquad \text{(Equation 2)}$$

By using the CALMAG and CIA-K weathering index calculation and the relationship established by Nordt and Driese (2010) for CALMAG and by Maynard (1992) for CIA-K, mean annual precipitation can be calculated using relationship established by Nordt & Driese (2010) for CALMAG and by Sheldon et al (2002) for CIA-K:

$$MAP = 22.69*(CALMAG) - 435.8 \qquad \text{(Equation 3)}$$

$$MAP = 14.3*(CIA\text{-}K) - 37.6 \qquad \text{(Equation 4)}$$

Ancient pCO_2 levels were estimated using C-isotope values derived from pedogenic carbonates and disseminated organic materials found in paleosols. The diffusion – production equation which models the contributions of atmospheric and soil respired CO_2 in the soil profile was used to calculate the concentration of CO_2 in the atmosphere (Cerling et al., 1991; Ekart et al., 1999):

$$pCO_2 = S(z)[(\delta^{13}C_s - 1.0044 * \delta^{13}C_r - 4.4) \div (\delta^{13}C_{atm} - \delta^{13}C_s)] \quad \text{(Equation 5)}$$

Where S(z) is the concentration of CO_2 from soil respired CO_2, $\delta^{13}C_s$ is the C-isotopic composition of soil CO_2, $\delta^{13}C_r$ is the C-isotopic composition of soil respired CO_2, and $\delta^{13}C_{atm}$ is the C-isotopic composition of the atmosphere. The S(z) value is a measure of soil productivity, the biological contribution of CO_2 to the soil in combination with atmospheric CO_2 contribution (Cerling et al., 1991; Cotton & Sheldon, 2012; Ekart et al., 1999). S(z) is a depth dependent contribution from soil-respired CO_2, and is by far the most significant factor on pCO_2 calculation, but also is the least well-constrained value in geologic materials (Cerling et al., 1991, 1993; Cotton & Sheldon, 2012; Ekart et al., 1999). S(z) has been estimated in several ways (e.g. Cotton & Sheldon, 2012; Ekart et al., 1999; Montañez, 2013) and is seen to be highly influenced by precipitation. For this study we used both a moderate estimate of S(z) = 2000 ppm, a high estimate of 3000 ppm, and a low estimate of 1000 ppm, with S(z) values from modern vertisols by Montañez (2013).

The isotopic composition of total CO_2 ($\delta^{13}C_s$) is determined from the isotopic composition of carbonate carbon. The low temperature value was assumed from Ekart et al. (1999) for soils in subtropical to temperate conditions at 25°C. The isotopic composition of respired CO_2 ($\delta^{13}C_r$) is estimated from occluded organic C within the carbonate nodules. The isotopic composition of the atmosphere ($\delta^{13}C_{atm}$) is determined in three ways. 1) The Arens et

al., (2000) method which relates the isotopic composition of organic matter to the isotopic composition of atmospheric CO_2

$$\delta^{13}C_{atm} = (\delta^{13}C_{org}+18.67) \div 1.10 \quad \text{(Equation 6)}$$

2) $\delta^{13}C_{atm}$ can be inferred from the $\delta^{13}C_{carb}$ of average of marine carbonates from the same age from Ekart et al (1999).

$$\delta^{13}C_{atm}= (\text{avg } \delta^{13}C_{\text{ Cretaceous marine carb}} -8) \quad \text{(Equation 7)}$$

Ekart et al (1999) used an average $\delta^{13}C_{atm}$ for Cloverly Formation pedogenic carbonates of +2.3‰ and calculated a $\delta^{13}C_{atm}$ of -5.7‰. 3). Finally, $\delta^{13}C_{atm}$ values may be calculated using temperature dependent fractionation factors established by fish $\delta^{18}O_{PO4}$ and the isotopic composition of marine carbonates from Barral et al. (2017) in which Late Aptian $\delta^{13}C_{atm}$ = -4.88‰.

These values and values calculated for mean annual precipitation were placed within a high-resolution, bulk organic C-isotopic chemostratigraphic profile constrained by detrital zircon geochronology from previous studies e.g D'Emic et al. (2019) and Carrano et al. (2021).

Results:

C-isotope chemostratigraphy

Three-point average values of the chemostratigraphic data were plotted against the stratigraphic section to show smoothed trends in the bulk $\delta^{13}C_{org}$ signal (Figure 3). C-isotope values range between -21‰ and -30.1‰ and average at -23.97‰. The produced bulk $\delta^{13}C_{org}$ curve was divided into seven segments. In the first segment, segment a, a PCIE exists in the Pryor Conglomerate and progresses into the Lower LSM Member with its peak at -20.88‰ at 15m. Segment b is characterized by a slight decreasing trend in $\delta^{13}C$ value to a minimum of -26.41‰ at 20.25m. Segment c is characterized by a rapid increase in $\delta^{13}C$ to -22.9‰ at 20.5 m. Segment d represents a persistent positive C-isotope trend for 7.5 m with an average value of -23.25‰. Segment e represents a negative C-isotope excursion from -22.87‰ at 28 m to -27.48‰ at 33.5 m in the lower portion of Himes Member (Unit VI). Segment f progresses as a positive CIE mainly in the bone bed of the Lower Himes Member (Unit VI) from 33.5m to a maximum of -23.32 at 36.55m. Finally, segment g, Upper Himes (Unit VII) maintains a gradual PCIE trend above the bone bed with some alternating NCIE's within the section and into the Sykes Mountain Formation.

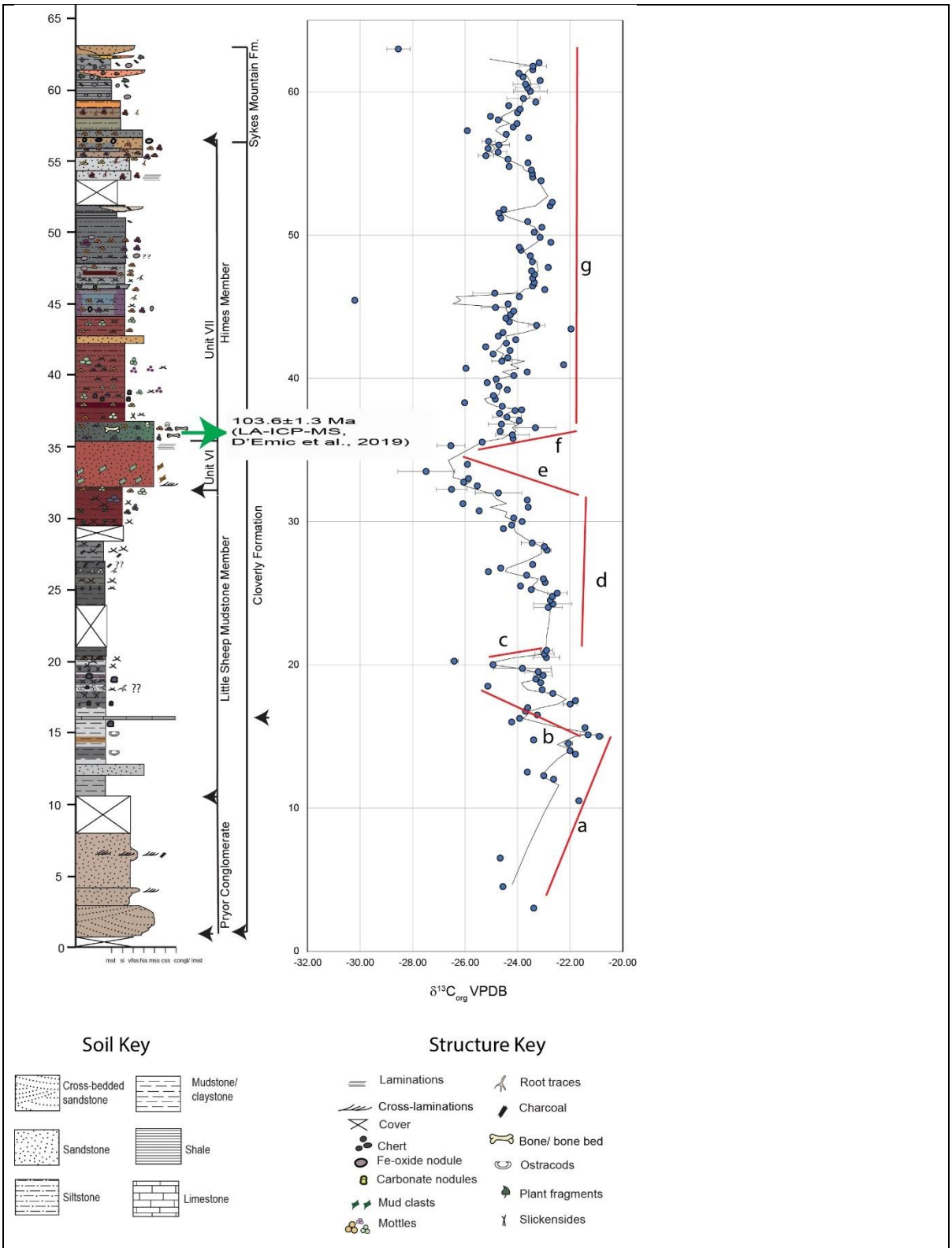

Figure 3: High resolution chemostratigraphic section and stratigraphic location of Cloverly samples showing segments a to g

Carbonate Petrography and Stable Isotope Analysis

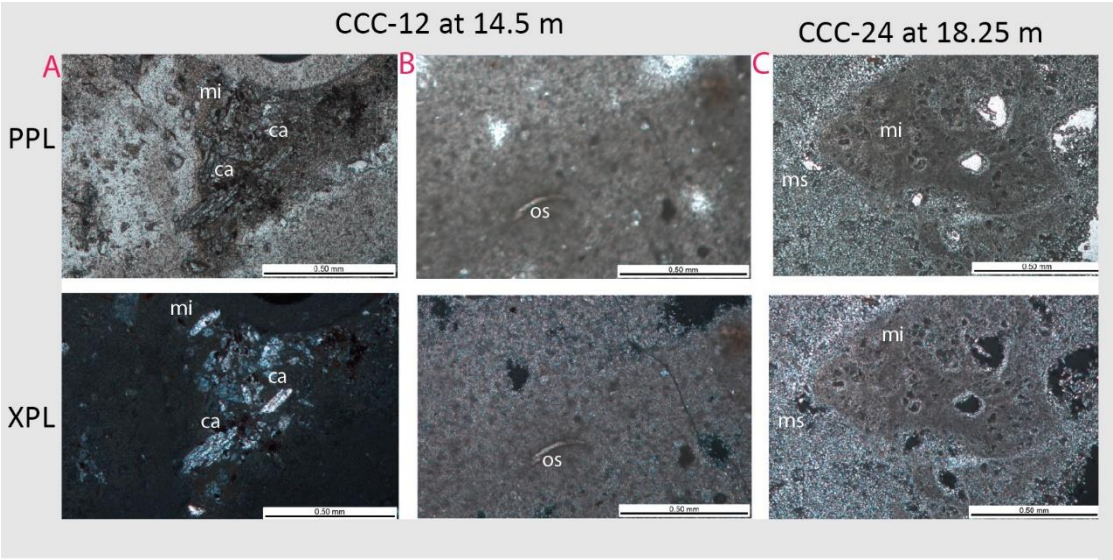

Figure 4: Photomicrographic image of carbonate nodules from the Little Sheep Mudstone Member shown in plane polarized (upper row) and cross polarized (lower row) light and taken at 10x magnification. (a) CCC-12 showing micrite and calcite rhombs. (b) CCC-12 showing micrite and microspar as well as an ostracode valve. (c) CCC-24 showing micrite and microspar with phreatic zone sparry linings of the micrite.

Abbreviations-mi-micrite, ca-calcite, os- ostracod, ms-micro spar, sp = spar

The pedogenic carbonates from the LSM predominantly preserve micritic textures. Micritic phases seen in the two samples are the primary phases of calcite. However, the micro spar present may be due to replacement of the original calcite or recrystallization from micrite within the phreatic zone. For example, CCC-24 (Figure 4c) shows phreatic zone spar lining the micrite within groundmass of micro spar. The micritic and micro-sparry portions were sampled, but only averages from the micrite were used for the pCO_2 calculation (Table 1, Figure 5). The sampled micrites in the Little Sheep Mudstone Member carbonate nodules have average $\delta^{13}C_{carb}$ value of -6.72 ‰ VPDB at CCC-12 and -7.25 ‰ VPDB at CCC-24. The average $\delta^{18}O_{carb}$ are -8.48 ‰ VPDB for CCC-12 and -7.96 ‰ VPDB at CCC-24. The average $\delta^{13}C_{carb}$ micro-sparry

values are -6.73 ‰ for CCC-12 and -7.22 ‰ for CCC-24. The average $\delta^{18}O_{carb}$ micro-sparry values are -8.64 for CCC-12, and -7.94 for CCC-24. The micrites have median $\delta^{13}C_{carb}$ values of -6.71 ‰ VPDB at CCC-12 and -7.24 ‰ VPDB at CCC-24. The median $\delta^{18}O_{carb}$ values are -8.46 ‰ VPDB for CCC-12 and -7.92 ‰ VPDB at CCC-24. The median $\delta^{13}C_{carb}$ micro-sparry values are -6.77 ‰ for CCC-12 and -7.20 ‰ for CCC-24. The median $\delta^{18}O_{carb}$ micro-sparry values are -8.61 for CCC-12, and -7.95 for CCC-24. The median and mean micrite and micro-sparry values are not significantly different from each other. This suggests there is no isotopic difference between the solution that precipitated the micrite and the microspar and suggests that the microspar may be the result of crystal coarsening and no fractionation occurred during crystal coarsening. In the absence of other diagenetic evidence, we suggest that the carbon and oxygen isotope compositions represent meteoric water during soil formation.

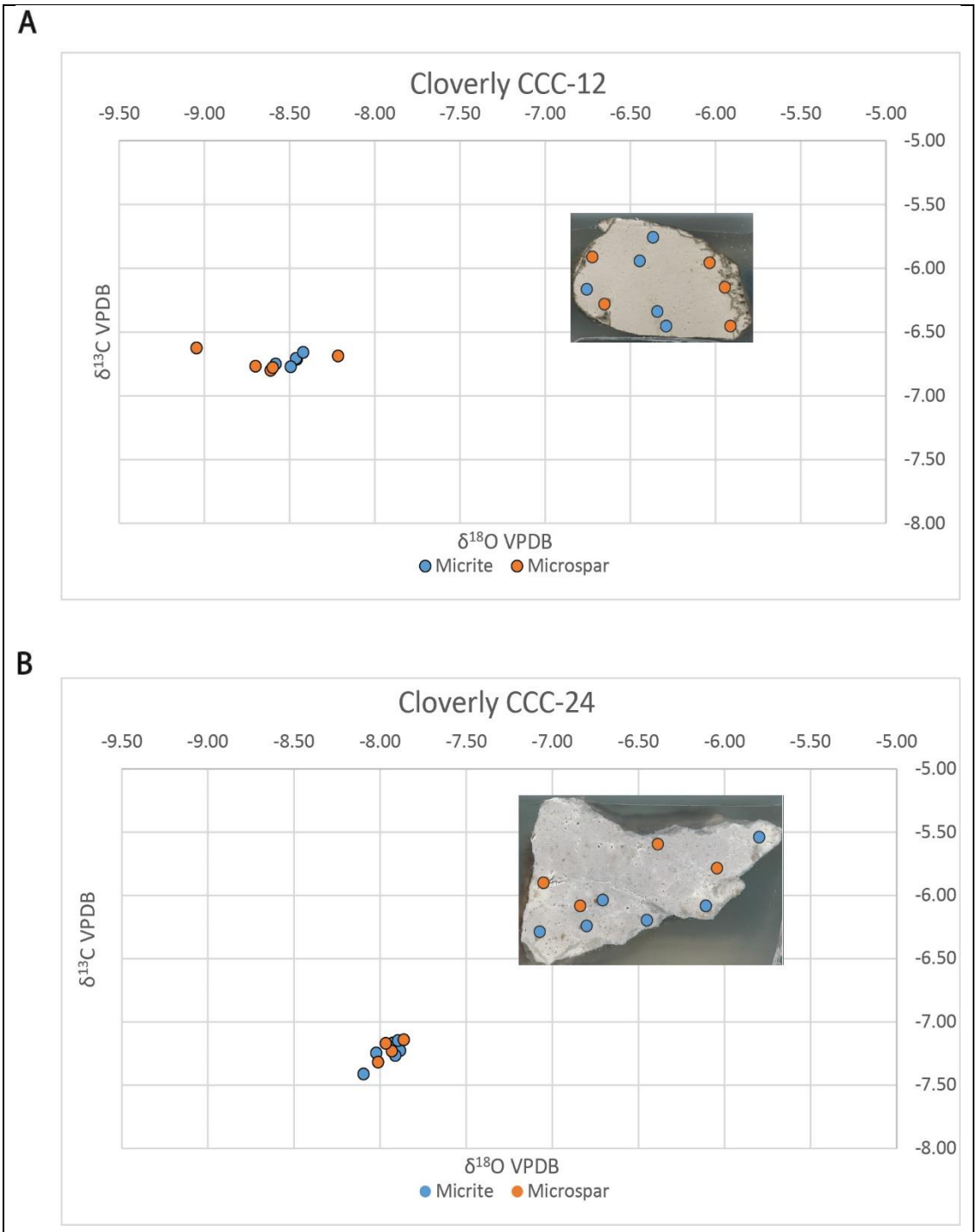

Figure 5**:** *C-O-isotope cross plot of CCC-12 (a) and CCC-24 (b) nodules. Blue color denotes micritic calcite, and orange color denotes microsparry calcite.*

Table 1: Characteristics of sampled areas for CCC-12 and CCC-24 carbonate nodules			
Samples	**Characteristics**	**$\delta^{13}C$ VPDB**	**$\delta^{18}O$ VPDB**
CCC-12_1	White micrite	-6.71	-8.45
CCC-12_2	White micrite	-6.71	-8.46
CCC-12_3	Light gray micrite	-6.77	-8.49
CCC-12_4	Light gray micrite	-6.66	-8.42
CCC-12_5	Sparry vein	-6.62	-9.04
CCC-12_6	Sparry vein	-6.80	-8.61
CCC-12_7	Sparry vein	-6.78	-8.59
CCC-12_8	Sparry vein	-6.69	-8.21
CCC-12_9	Sparry vein	-6.77	-8.69
CCC-12_10	Light gray micrite	-6.75	-8.58
CCC-24_1	Dark gray micrite	-7.17	-7.93
CCC-24_2	Dark gray micrite	-7.41	-8.09
CCC-24_3	Dark gray micrite	-7.25	-8.02
CCC-24_4	Dark gray micrite	-7.23	-7.88
CCC-24_5	Light gray micrite	-7.27	-7.91
CCC-24_6	Sparry	-7.14	-7.86
CCC-24_7	Light gray micrite	-7.15	-7.89
CCC-24_8	Sparry	-7.23	-7.93
CCC-24_9	Sparry	-7.32	-8.01
CCC-24_10	Sparry	-7.17	-7.96

pCO_2 Calculations

Atmospheric pCO_2 calculations use the paleosol pCO_2 paleobarometer of Ekart et al. (1999). In this relationship, $\delta^{18}O_{org}$ and $\delta^{18}O_{carb}$ are used to estimate the concentration of pCO_2 within a soil in equilibrium with the atmosphere. The temperature of formation of carbonate, the isotopic composition of the atmosphere, and the concentration of soil respired CO_2 (S(z)) are all unknowns that must either be estimated using other proxies or assumed. We assumed a temperature of 25°C for formation of carbonates. The isotopic composition of the atmospheric CO_2 was estimate in three ways: 1) using equation 6 in which the isotopic composition of bulk organic C of occluded organic material from the carbonate nodule is used to calculate $\delta^{13}C_{atm}$ (Arens et al., 2000). 2) The average isotopic composition of marine carbonates is assumed to be

in equilibrium with the atmosphere and is used to calculate the isotopic composition of the atmosphere (Ekart et al., 1999). We used the average value for Early Cretaceous marine carbonates reported by Ekart et al. (1999) of -5.7‰. 3) Barral et al. (2017) generates a more accurate $\delta^{13}C_{atm}$ by determining the temperature dependent fractionation factor (ε) between DIC and CO_2 for different time slices. Temperature is estimated from fish phosphate from the same interval and used to determine these fractionation factors. These fractionation factors are then used in conjunction with the average marine carbonate values for the desired time slice to calculate a more accurate $\delta^{13}C_{atm}$. For the Late Aptian time slice, $\delta^{13}C_{atm}$= -4.88‰ (Barral et al., 2017). S(z) values can be estimated using MAP and the relationship established by Cotton & Sheldon (2012), but their relationship is best used for low MAP values (150 to 600 mm/yr) and MAP calculated from our data suggests that the MAP is much greater for the Cloverly (see below). Thus, we estimated S(z) values using the range of vertic soil estimates from Montañez. (2013). Table 2 shows the range in pCO_2 values calculated using the variety of $\delta^{13}C_{atm}$ and S(z) values.

Using the Arens et al., (2000) estimation for $\delta^{13}C_{atm}$, atmospheric pCO_2 values at 14.5 m above the Morrison – Cloverly contact are 352 ± 176 ppm at 14.5 m and increase to 931 ± 465 ppm at 18.5 m. Using Ekart et al., (1999), results for 14.5 m above the Morrison – Cloverly contact are 446 ± 223 ppm and increase to 916 ± 458 ppm at 18.5 m. Using Barral et al. (2017), atmospheric pCO_2 values at 14.5 m above the Morrison – Cloverly contact are 411 ± 205 ppm at 14.5 m and increase to 849 ± 424 ppm at 18.5 m.

Table 2: Atmospheric $\delta^{13}C_{atm}$ calculations from (Arens et al., 2000; Barral et al., 2017; Ekart et al., 1999) for CCC-12 and CCC-24 using isotopic composition of organic C mudstone and carbonate carbon				
Atmospheric $\delta^{13}C_{atm}$ = -5.7 ‰ (Ekart et al., 1999) for both samples				
Sample (Mudstone)	pCO_2 at Sz = 1000 ppm	pCO_2 at Sz = 2000 ppm	pCO_2 at Sz = 3000 ppm	pCO_2 @ Sz = 5000 ppm (used by Ekart 1999)
CCC-12 @ 14.5 m	223	446	668	1114
CCC-24 @ 18.5 m	458	916	1373	2289
Atmospheric $\delta^{13}C_{atm}$ = -6.9 ‰ (Arens et al., 2000) for CCC-12 and δ^{13}Catm = -6.63 ‰ for CCC-24				
CCC-12 @ 14.5 m	176	352	528	880
CCC-24 @ 18.5 m	465	931	1397	2328
Atmospheric $\delta^{13}C_{atm}$ = -4.88‰ (Barral et al., 2017) for both samples				
CCC-12 @ 14.5 m	205	411	617	1028
CCC-24 @ 18.5 m	424	849	1273	2121

Mean Annual Precipitation

MAP calculations are reported in Table 3 with CALMAG and CIA-K (also see Figure 7). MAP increases up section from a minimum of 697– 984 mm/yr in the Little Sheep Mudstone Member to a maximum of 1291 – 1705 mm/yr in the upper Himes Member.

Table 3: MAP calculated with CALMAG and CIA-K for micro-high vertic soils			
Sample	Meters above Morrison Fm.	MAP from CALMAG (mm/yr)	MAP from CIA-K (mm/yr)
CCC-18	16.75	1195	857
CCC-22	17.75	984	696
CCC-29	19.50	1428	1098
CCC-31	20	1461	1117
CCC-43	26	1375	1002
CCC-52	29.75	1390	1076
CCC-59	31.75	1447	1132
CCC-78	38.05	1582	1145
CCC-79	38.30	1588	1172
CCC-106	45.20	1595	1220
CCC-120	49.15	1705	129
CCC-136	55.05	1680	127
CCC-144	57.05	1618	1241

Interpretation and Discussion:

Based on constraints from a volcanolithic tuff with an age of 112.09 ± 0.34 Ma determined from CA-ID-TIMS (Carrano et al., 2021) from Little Sheep Mudstone Member outcrops near Shell, Wyoming, and a maximum depositional age of 103.6 ± 1.3 Ma generated from LA-ICP-MS (D'Emic et al., 2019) from the Crooked Creek Section within the lower Himes Member, the C-isotope record can be compared to the global C-isotope record from ~ 115 to ~ 100 Ma (Figure 6). We correlated the C-isotope record from the Cloverly to that of the $\delta^{13}C_{carb}$ of Bralower et al. (1999); Herrle et al. (2015) and the $\delta^{13}C_{org}$ record from the Ruby Ranch Member of the Cedar Mountain Formation of Utah from Gottberg (2022) (Figure 6). The $\delta^{13}C_{org}$ trend within the lower LSM Member in which the ascending limb of segment a to the end of segment e with a broad positive C-isotope maximum of -22.49 % was cautiously correlated to the positive C-isotope trend C-9, persistent positive C-isotope trend (C-10), and decreasing negative trend (C-11) of Bralower et al. (1999) (Figure 6). This places the correlation to fall within the ages of

114-108 Ma for the Upper Little Sheep Mudstone Member and the lower Himes Member. This is a tentative correlation, because the maximum depositional age of 103.6 ± 1.3 Ma occurs at the bone-bearing unit starting at 35.55m and the minimum point of segment e for which we correlate to the C-11 segment of Bralower et al. (1999) has a known age of ~ 109 Ma at 33.5m. Thus, only 2.05 m would be deposited within 5.4 million years. For this correlation to be valid, a significant unconformity would have occurred within this interval, or the 103.6 Ma date generated from LA-ICP-MS may have been affected by lead loss causing a younger age calculation, or our correlation in not valid.

Just below the bone bed at ~32.25m there are mudstone rip-up clasts and ripple marks. The detrital zircon sample from within the bone bed is within a fluvial sandstone body that could have many instances of unconformities. In general, D'Emic et al. (2019) and others (e.g. Elliott et al., 2007; Way et al., 1998) suggest that the Little Sheep Mudstone Member has persistent unconformities with ~15 million years being represented in ~40 m of the sections in southwest Cody and Shell Wyoming. Thus, a significant unconformity could be possible.

Lead loss is another possibility for the age mismatch. Lead loss occurs when a damaged part of the zircon crystal matrix results in a loss of lead and a younger calculated age when using LA-ICP-MS spot techniques (Herrmann et al., 2021; Zi et al., 2022). This effect has been observed by several authors (Gehrels et al., 2020; Herriott et al., 2019; Quadt et al., 2014). Chemical abrasion ID-TIMS removes these damaged portions and results in an older age than those calculated by LA-ICP-MS. Significant lead loss that results in an age calculation of at least 5.4 Ma younger than the C-isotope correlated age of 109 Ma (minimum of the C-11 segment) as opposed to the reported age of D'Emic et al. (2019) could be the result of analysis via LA-

ICPMS as opposed to CA-ID-TIMS. Thus, U-Pb detrital zircon geochronology with CA-ID-TIMS, will present more accurate and precise dates (Quadt et al., 2014).

Alternative correlations are difficult to make, because there is a clear negative CIE made up of segments e and f, with a magnitude of -4.16‰. There are few negative CIEs with a similar magnitude within 105 to 100 Ma that would correlate to this excursion within the known global C-isotope record for this period. It is possible that the excursion represents a local change in source organic material, but without compound specific isotope analysis of long-chain alkanes such a determination is not possible.

In general, the C-10 interval has been associated with the Southern Kerguelen LIP (Bottini et al., 2015; Erba et al., 2015; Herrle et al., 2015). Within the C-9 to C-11 excursions, short-lived events have been documented, for example the Kilian, Jacob, and OAE 1b events. More specifically, the Jacob and Kilian event have been associated with cooling and warming, respectively. Given our climate data (see below), we correlate the peak $\delta^{13}C_{org}$ of segment a to the Jacob event seen in Herrle et al. (2015) and the peak of the negative excursion in segment b to the Kilian Event. This correlation is supported by known climatic events associated with each and our data (e.g., Bracquart et al., 2022; Weissert et al., 1998).

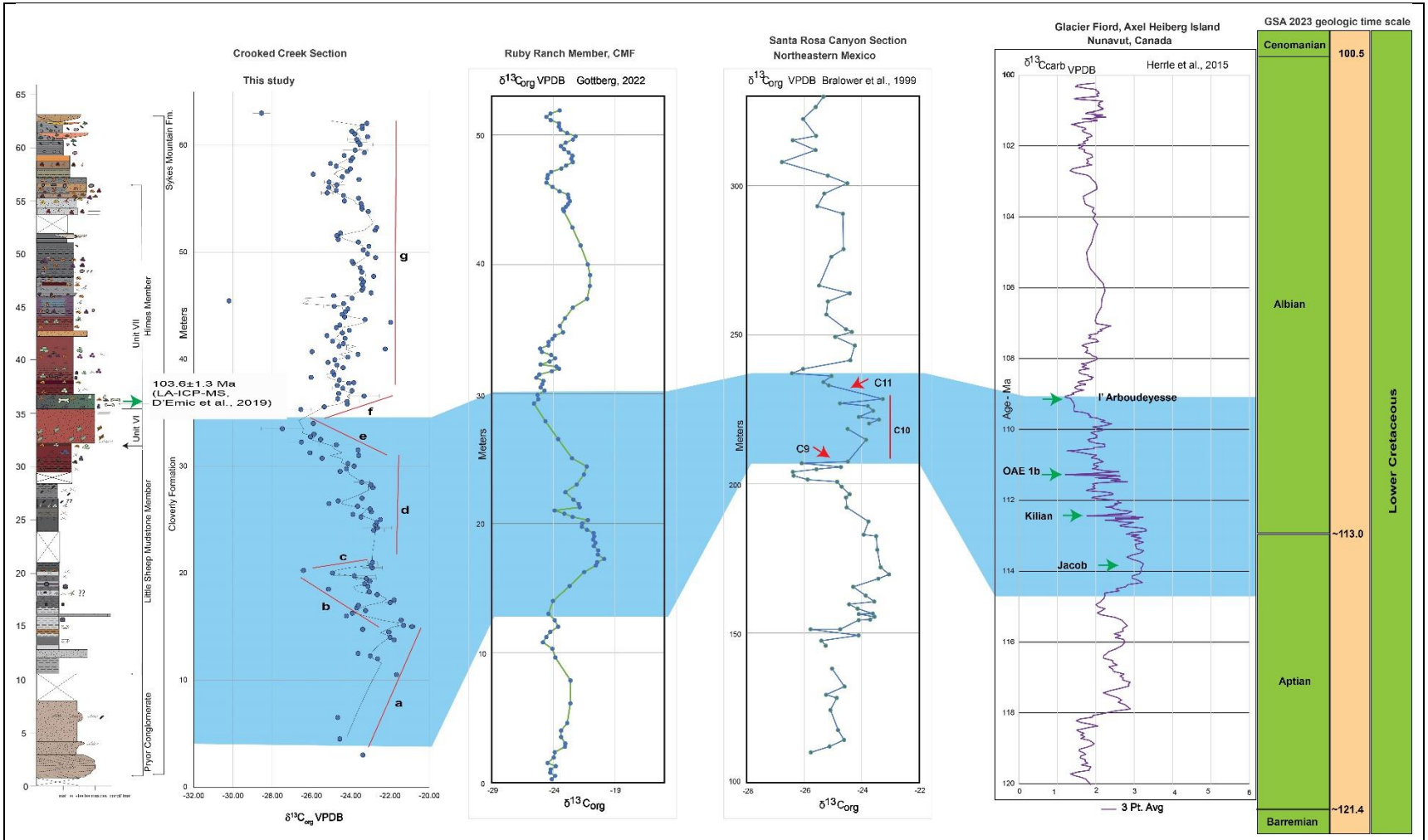

Figure 6: High resolution stratigraphic section, Crooked Creek $\delta^{13}C_{org}$, Gottberg (2022*)* $\delta^{13}C_{org}$, Bralower et al. (1999) $\delta^{13}C_{org}$, Herrle et al. (2015) $\delta^{13}C_{carb.}$ *Also showing* D'Emic et al. (2019) *LA-1CPMS detrital zircon geochronology age of MDA of 103.6 ± 1.3 Ma in the Himes Member*

The presence of dispersed volcanic ash from the subaerial southern Kerguelen eruption, glenodites from the same time period in high-latitudes, foraminiferal zones such as *Globoginerlloides alerianus*, *Ticinella bejaouaensis*, high latitude ice-rafted debris, enhanced delivery of terrestrial organic matter, sea-level low stand, and increased weathering rates are linked to the Jacob peak cold snap (Erba et al., 2015; Herrle et al., 2015; Hochuli et al., 1999; Leckie et al., 2002). Our climate data (Figure 7) supports this correlation in which an increasing trend of pCO_2 values from 352 ± 176 ppm for CCC-12 to 931± 465 ppm for CCC-24 is observed. The Kilian event (112.5 Ma) is associated with the start of renewed warming and black shales (Herrle et al., 2015; McAnena et al., 2013). This correlation with the Kilian event and its associated warming is supported by our MAP data in which MAP increases rapidly following the peak negative excursion of segment b. Increasing MAP is often associated with increasing temperatures in which a warmer atmosphere can hold more water, resulting in intensification of the hydrological cycle.

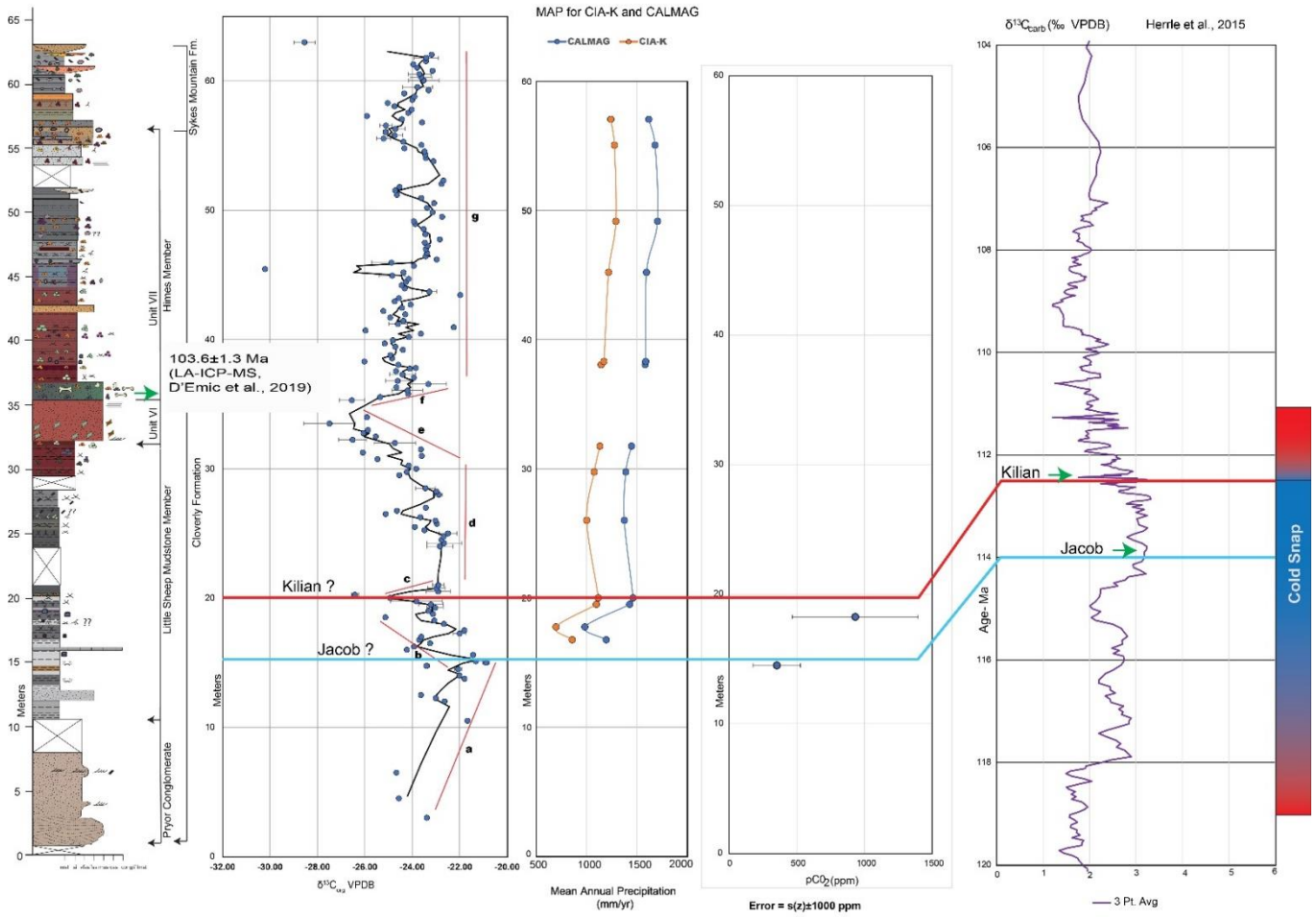

Figure 7: *Stratigraphic section, chemostratigraphic curve, pCO_2 calculations from pedogenic carbonate nodules and $\delta^{13}C_{org}$ of mudstone and MAP calculations from CALMAG (Nordt & Driese, 2010) and CIA-K (Sheldon et al., 2002) from Crooked Creek Section, Cloverly Formation*

Cotton & Sheldon. (2012) suggest that $\Delta^{13}C$ ($\delta^{13}C_{carb}$- $\delta^{13}C_{org}$) should range between 14‰ and 17‰ for organic C from the occluded organic matter and $\delta^{13}C_{carb}$ suggesting equilibrium between the two organic C sources. In our calculations, however, we calculated the pCO_2 using bulk organic C from mudstones. We further investigated pCO_2 values by calculating $\Delta^{13}C$ ($\delta^{13}C_{carb}$- $\delta^{13}C_{occluded\ organic\ C}$) from the occluded organic C within pedogenic carbonate nodules. Our calculated data using the occluded organic matter falls outside the range of $\Delta^{13}C$ suggesting the $\delta^{13}C_{occluded\ organic\ C}$ and pedogenic carbonate $\delta^{13}C_{carb}$ are out of equilibrium (Table 4). We calculated $\Delta^{13}C$ using bulk organic C from mudstones and $\delta^{13}C_{carb}$. This results in $\Delta^{13}C$ values falling within the suggested 14-17‰ range implying equilibrium with a slightly off value for CCC-24 calculated as 17.82‰ (Table 4). Values from the $\delta^{13}C_{occluded\ organic\ C}$ and pedogenic carbonate $\delta^{13}C_{carb}$ does not correspond with our interpretation of associated Jacob and Kilian events (Table 5, Figure 8). Using Arens et al. (2000) estimation for $\Delta^{13}C_a$, atmospheric pCO_2 values at 14.5 m above the Cloverly-Morrison Formation contact are 1484 ± 742 ppm and decrease to 1185 ± 592 ppm at 18.5 m. Using Ekart et al. (1999), atmospheric pCO_2 values at 14.5 m above the Morrison-Cloverly contact are 1301 ± 651 ppm at 14.5 m and decrease to 1078 ± 539 ppm at 18.5 m. Using Barral et al., (2017), atmospheric pCO_2 at 14.5 m above the Morrison-Cloverly contact are 1203 ± 602 ppm and decrease to 999 ± 500 ppm at 18.5 m. However, for the calculated $\delta^{13}C_{mudstone\ organic\ C}$ and pedogenic carbonate $\delta^{13}C_{carb}$, there is an increase in pCO_2 from 14.5 to 18.5 m. of about 2x. (Figure 7). Atmospheric pCO_2 doubles just prior to what we interpret as the Kilian Event (and its associated warming) and just prior to an increase in MAP in the Crooked Creek section. This trend would be consistent with low pCO_2 during the Cold Snap associated with the Jacob Event and increase in pCO_2 and warming during the Kilian Event. Although recent work suggests that occluded organic matter from within the

carbonate nodules should be used when calculating pCO_2 (Cotton & Sheldon, 2012; Montañez, 2013; Porter et al., 2017), we suggest that the pCO_2 trends associated with values calculated using isotopic composition of bulk organic C in mudstones are valid. These pCO_2 values are still within the range of values seen in other studies for this time period e.g Aptian pCO_2 concentrations of 1000 – 2000 ppm with a minimum of ~450 ppm specifically in the Late Aptian based on Gradstein et al., (2012) time scale (Hong & Lee, 2012; Li et al., 2014).

Table 4: $\Delta^{13}C$ range of $\delta^{13}C_{org}$ of mudstone and $\delta^{13}C_{org}$ of occluded organic material		
$\delta^{13}C_{org}$	$\Delta^{13}C$ ($\delta^{13}C_c$- $\delta^{13}C_{org}$)	Carbonate Nodule
$\delta^{13}C_{org}$ of mudstone	15.34	CCC-12
	17.88	CCC-24
$\delta^{13}C_{org}$ of occluded organic material	19.55	CCC-12
	18.72	CCC-24

Table 5: Atmospheric $\delta^{13}C_{atm}$ calculations from (Arens et al., 2000; Barral et al., 2017; Ekart et al., 1999) CCC-12 and CCC-24 from the $\delta^{13}C_{occluded\ organic\ C}$ and pedogenic carbonate $\delta^{13}C_{carb}$				
Atmospheric $\delta^{13}C_{atm}$ = -5.7 ‰ from Ekart et al. (1999) for both samples				
Sample (occluded organic matter)	pCO_2 at Sz = 1000 ppm	pCO_2 at Sz = 2000 ppm	pCO_2 at Sz = 3000 ppm	pCO_2 @ Sz = 5000 ppm (used by Ekart 1999)
CCC-12 @ 14.5 m	651	1303	1955	3258
CCC-24 @ 18.5 m	539	1078	1617	2695
Atmospheric $\delta^{13}C_{atm}$ = -6.9 ‰ from Arens et al. (2000) for CCC-12 and δ^{13}Catm = -6.63 ‰ for CCC-24				
CCC-12 @ 14.5 m	742	1485	2228	3714
CCC-24 @ 18.5 m	592	1185	1777	2962
Atmospheric $\delta^{13}C_{atm}$ = -4.88‰ from Barral et al. (2017) for both samples				
CCC-12 @ 14.5 m	602	1203	1805	3008
CCC-24 @ 18.5 m	500	999	1499	2498

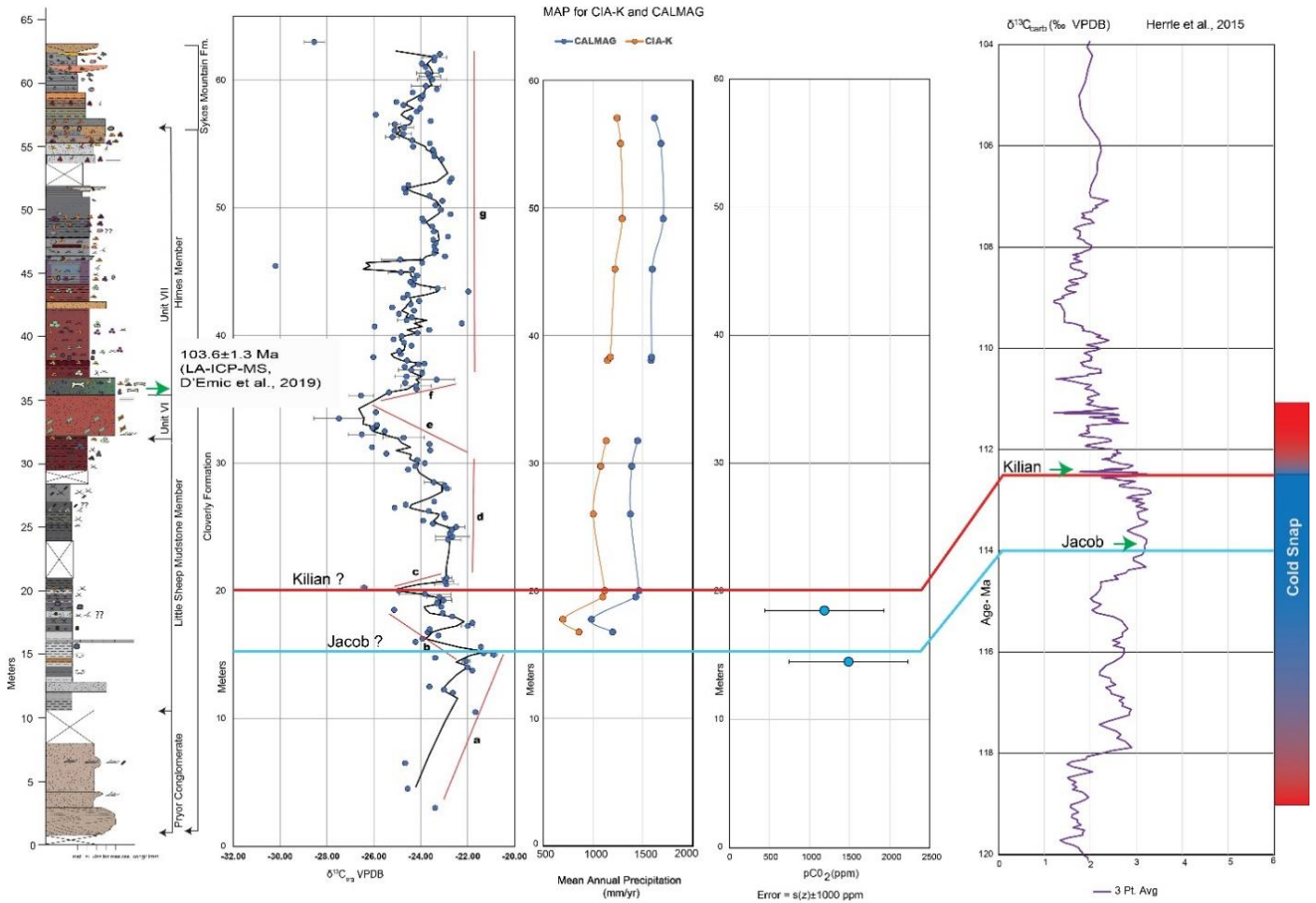

Figure 8: Stratigraphic section, chemostratigraphic curve, pCO_2 calculations from $\delta^{13}C_{occluded\ organic\ C}$ and pedogenic carbonate $\delta^{13}C_{carb}$ nodules, and MAP calculations from CALMAG (Nordt & Driese, 2010) and CIA-K (Sheldon et al., 2002) *at the Crooked Creek Section, Cloverly Formation*

Conclusion

Interpreting the climatic conditions of the Early – Late Cretaceous climate has posed several challenges to paleontologists, geochemists, and stratigraphers. However, stable isotope analysis of $\delta^{13}C_{org}$, $\delta^{13}C_{carb}$, paleoatmospheric CO_2 calculations, and mean annual precipitations calculations are helpful proxies for interpreting the terrestrial Cretaceous history. We analyzed the record of climatic events in the Crooked Creek Section of the Cloverly Formation through chemostratigraphic sampling in the field, stable isotope analyses of bulk organic and pedogenic carbonates preserved in vertic soils, thin sections, and weight percent oxide analyses of vertic soils. Our high-resolution bulk organic C-isotope chemostratigraphic profile placed the pCO_2 values in a higher resolution chronostratigraphic location. Given the maximum depositional age of the Little Sheep Mudstone Member (129.4 ± 0.12 Ma) from D'Emic et al. (2019) and a maximum depositional age for the lower Himes Member at Crooked Creek of 103.6 ± 1.3 Ma (D'Emic et al., 2019), we constrained the broad PCIE to the C-9 to C-11 segments of Bralower et al. (1999); McAnena et al. (2013), and others. More specifically, we correlated segment a of this study to the Jacob event, and the negative isotope excursion of segment b to the Kilian event. The low pCO_2 values are consistent with the "Cold Snap" associated with the Jacob Event. This cold snap is interpreted to be the result of subaerial eruption of the Kerguelen LIP in the southern hemisphere in which increased nutrients released to the ocean and ashy eruptions resulted in an increase in terrestrial burial of organic matter and combined to result in global cooling (Erba et al., 2015; McAnena et al., 2013). Following the interpreted Kilian event, the mean annual precipitation values show an increase up section (Figure 7). This increasing MAP is consistent with lithology from the Crooked Creek Section as evidenced by intense mottling and slickensides. This is also consistent with a doubling in pCO_2 at 18.5 m, resulting in increased

greenhouse warming and resulting in an intensification of the hydrological cycle as evident in the MAP data. Future detrital zircon U-Pb analysis (CA-ID-TIMS age) of the Cloverly Formation is recommended for precision and accuracy of zircon dates from the Crooked Creek section to resolve substantial parts with lead loss and reduce data scatter. This will be helpful to confirm correlations to the C-isotope record interpreted here and will better constrain the age of the Cloverly Formation and its correlation to other fauna of the Western Interior Basin.

References:

Almeida, V. V., Janasi, V. A., Heaman, L. M., Shaulis, B. J., Hollanda, M. H. B. M., & Renne, P. R. (2018). Contemporaneous alkaline and tholeiitic magmatism in the Ponta Grossa Arch, Paraná-Etendeka Magmatic Province: Constraints from U–Pb zircon/baddeleyite and 40 Ar/ 39 Ar phlogopite dating of the José Fernandes Gabbro and mafic dykes. *Journal of Volcanology and Geothermal Research*, *355*, 55–65. https://doi.org/10.1016/j.jvolgeores.2017.01.018

Arens, N. C., & Jahren, A. H. (2000). Carbon Isotope Excursion in Atmospheric CO2 at the Cretaceous-Tertiary Boundary: Evidence from Terrestrial Sediments. *PALAIOS*, *15*(4), 314–322. https://doi.org/10.1669/0883-1351(2000)015<0314:CIEIAC>2.0.CO;2

Arens, N. C., Jahren, A. H., & Amundson, R. (2000). Can C3 plants faithfully record the carbon isotopic composition of atmospheric carbon dioxide? *Paleobiology*, *26*(1), 137–164. https://doi.org/10.1666/0094-8373(2000)026<0137:CCPFRT>2.0.CO;2

Arthur, M. A., Dean, W. E., & Pratt, L. M. (1988). Geochemical and climatic effects of increased marine organic carbon burial at the Cenomanian/Turonian boundary. *Nature*, *335*(6192), 714–717.

Ballentine, D. C., Macko, S. A., & Turekian, V. C. (1998). Variability of stable carbon isotopic compositions in individual fatty acids from combustion of C4 and C3 plants: Implications for biomass burning. *Chemical Geology*, *152*(1–2), 151–161. https://doi.org/10.1016/S0009-2541(98)00103-X

Barral, A., Gomez, B., Legendre, S., & Lécuyer, C. (2017). Evolution of the carbon isotope composition of atmospheric CO2 throughout the Cretaceous. *Palaeogeography,*

Palaeoclimatology, Palaeoecology, *471*, 40–47. https://doi.org/10.1016/j.palaeo.2017.01.034

Bodin, S., Meissner, P., Janssen, N. M. M., Steuber, T., & Mutterlose, J. (2015). Large igneous provinces and organic carbon burial: Controls on global temperature and continental weathering during the Early Cretaceous. *Global and Planetary Change*, *133*, 238–253. https://doi.org/10.1016/j.gloplacha.2015.09.001

Bond, D. P. G., & Wignall, P. B. (2014). Large igneous provinces and mass extinctions: An update. In G. Keller & A. C. Kerr, *Volcanism, Impacts, and Mass Extinctions: Causes and Effects*. Geological Society of America. https://doi.org/10.1130/2014.2505(02)

Bottini, C., Erba, E., Tiraboschi, D., Jenkyns, H. C., Schouten, S., & Sinninghe Damsté, J. S. (2015). Climate variability and ocean fertility during the Aptian Stage. *Climate of the Past*, *11*(3), 383–402. https://doi.org/10.5194/cp-11-383-2015

Bracquart, E., Charbonnier, G., Garel, S., Munier, T., Adatte, T., & Danzelle, J. (2022). New evidences of subaerial volcanism as a trigger for the Kilian event (Aptian-Albian transition) and major climatic changes from offshore Morocco (DSDP Site 545). *Global and Planetary Change*, *218*, 103959. https://doi.org/10.1016/j.gloplacha.2022.103959

Bralower, T. J., CoBabe, E., Clement, B., Sliter, W. V., Osburn, C. L., & Longoria, J. (1999). The record of global change in mid-Cretaceous (Barremian-Albian) sections from the Sierra Madre, northeastern Mexico. *The Journal of Foraminiferal Research*, *29*(4), 418–437.

Breugel, Y. van. (2006). *Causes for negative carbon isotope anomalies in Mesozoic marine sediments: Constraints from modern and ancient anoxic settings: = Oorzaken van de negatieve koolstofisotoopexcursie in mariene sedimenten van het Mesozoïcum: lessen uit*

hedendaagse en vroegere anoxische milieus ; (met een samenvatting in het Nederlands). Univ.

Carrano, M. T., Oreska, M. P. J., Murch, A., Trujillo, K. C., & Chamberlain, K. R. (2021). Vertebrate paleontology of the Cloverly Formation (Lower Cretaceous), III: A new species of *Albanerpeton* , with biogeographic and paleoecological implications. *Journal of Vertebrate Paleontology*, *41*(5), e2003372. https://doi.org/10.1080/02724634.2021.2003372

Cerling, T. E., Solomon, D. K., Quade, J., & Bowman, J. R. (1991). On the isotopic composition of carbon in soil carbon dioxide. *Geochimica et Cosmochimica Acta*, *55*(11), 3403–3405. https://doi.org/10.1016/0016-7037(91)90498-T

Cerling, T. E., Wang, Y., & Quade, J. (1993). Expansion of C4 ecosystems as an indicator of global ecological change in the late Miocene. *Nature*, *361*(6410), Article 6410. https://doi.org/10.1038/361344a0

Coffin, M. F. (2002). Kerguelen Hotspot Magma Output since 130 Ma. *Journal of Petrology*, *43*(7), 1121–1137. https://doi.org/10.1093/petrology/43.7.1121

Cotton, J. M., & Sheldon, N. D. (2012). New constraints on using paleosols to reconstruct atmospheric pCO2. *Geological Society of America Bulletin*, *124*(9–10), 1411–1423. https://doi.org/10.1130/B30607.1

Cramer, B. D., & Jarvis, I. (2020). Chapter 11—Carbon Isotope Stratigraphy. In F. M. Gradstein, J. G. Ogg, M. D. Schmitz, & G. M. Ogg (Eds.), *Geologic Time Scale 2020* (pp. 309–343). Elsevier. https://doi.org/10.1016/B978-0-12-824360-2.00011-5

Cucciniello, C., Langone, A., Melluso, L., Morra, V., Mahoney, J. J., Meisel, T., & Tiepolo, M. (2010). *U-Pb Ages, Pb-Os Isotope Ratios, and Platinum-Group Element (PGE)*

Composition of the West-Central Madagascar Flood Basalt Province. https://doi.org/10.1086/655012

DeCelles, P. G. (2004). Late Jurassic to Eocene evolution of the Cordilleran thrust belt and foreland basin system, western U.S.A. *American Journal of Science*, *304*(2), 105–168. https://doi.org/10.2475/ajs.304.2.105

DeCelles, P. G., & Burden, E. T. (1992). Non-marine sedimentation in the overfilled part of the Jurassic-Cretaceous Cordilleran foreland basin: Morrison and Cloverly Formations, central Wyoming, USA. *Basin Research*, *4*(3–4), 291–314. https://doi.org/10.1111/j.1365-2117.1992.tb00050.x

D'Emic, M. D., Foreman, B. Z., Jud, N. A., Britt, B. B., Schmitz, M., & Crowley, J. L. (2019). Chronostratigraphic Revision of the Cloverly Formation (Lower Cretaceous, Western Interior, USA). *Bulletin of the Peabody Museum of Natural History*, *60*(1), 3. https://doi.org/10.3374/014.060.0101

Dong, C., Sun, B.-N., Wu, J.-Y., Du, B.-X., Xu, X.-H., & Jin, P.-H. (2014). Structure and affinities of Athrotaxites yumenensis sp. Nov. (Cupressaceae) from the Lower Cretaceous of northwestern China. *Cretaceous Research*, *47*, 25–38. https://doi.org/10.1016/j.cretres.2013.09.012

Ekart, D. D., Cerling, T. E., Montanez, I. P., & Tabor, N. J. (1999). A 400 million year carbon isotope record of pedogenic carbonate: Implications for paleoatmospheric carbon dioxide. *American Journal of Science*, *299*(10). https://doi.org/10.2475/ajs.299.10.805

Elliott, W. S., Suttner, L. J., & Pratt, L. M. (2007). Tectonically induced climate and its control on the distribution of depositional systems in a continental foreland basin, Cloverly and

Lakota Formations (Lower Cretaceous) of Wyoming, U.S.A. *Sedimentary Geology*, *202*(4), 730–753. https://doi.org/10.1016/j.sedgeo.2007.09.001

Erba, E., Duncan, R. A., Bottini, C., Tiraboschi, D., Weissert, H., Jenkyns, H. C., & Malinverno, A. (2015). Environmental consequences of Ontong Java Plateau and Kerguelen Plateau volcanism. In *Geological Society of America Special Papers* (Vol. 511, pp. 271–303). Geological Society of America. https://doi.org/10.1130/2015.2511(15)

Ernst, R. E., & Youbi, N. (2017). How Large Igneous Provinces affect global climate, sometimes cause mass extinctions, and represent natural markers in the geological record. *Palaeogeography, Palaeoclimatology, Palaeoecology*, *478*, 30–52. https://doi.org/10.1016/j.palaeo.2017.03.014

Florisbal, L. M., Heaman, L. M., De Assis Janasi, V., & De Fatima Bitencourt, M. (2014). Tectonic significance of the Florianópolis Dyke Swarm, Paraná–Etendeka Magmatic Province: A reappraisal based on precise U–Pb dating. *Journal of Volcanology and Geothermal Research*, *289*, 140–150. https://doi.org/10.1016/j.jvolgeores.2014.11.007

Foreman, B. Z., Heller, P. L., & Clementz, M. T. (2012). Fluvial response to abrupt global warming at the Palaeocene/Eocene boundary. *Nature*, *491*(7422), 92–95. https://doi.org/10.1038/nature11513

Frey, F. A., Coffin, M. F., Wallace, P. J., & Quilty, P. G. (Eds.). (2003). *Proceedings of the Ocean Drilling Program, 183 Scientific Results* (Vol. 183). Ocean Drilling Program. https://doi.org/10.2973/odp.proc.sr.183.2003

Furer, L. C. (1970). Petrology and Stratigraphy of Nonmarine Upper Jurassic-Lower Cretaceous Rocks of Western Wyoming and Southeastern Idaho1. *AAPG Bulletin*, *54*(12), 2282–2302. https://doi.org/10.1306/5D25CC91-16C1-11D7-8645000102C1865D

Gehrels, G., Giesler, D., Olsen, P., Kent, D., Marsh, A., Parker, W., Rasmussen, C., Mundil, R., Irmis, R., Geissman, J., & Lepre, C. (2020). LA-ICPMS U–Pb geochronology of detrital zircon grains from the Coconino, Moenkopi, and Chinle formations in the Petrified Forest National Park (Arizona). *Geochronology*, *2*(2), 257–282. https://doi.org/10.5194/gchron-2-257-2020

Gottberg, A. (2022). *Carbonate Carbon Isotope Chemostratigraphy from the Ruby Ranch Member of the Cedar Mountain Formation in the Western San Rafael Swell* [M.S., University of Kansas]. https://www.proquest.com/docview/2641563529/abstract/35173554B6A34449PQ/1

Gradstein, F., Ogg, J. G., Schmitz, M. D., & Ogg, G. M. (2012). *The Geologic Time Scale 2012*. Elsevier.

Grimaldi, D. (1999). The Co-Radiations of Pollinating Insects and Angiosperms in the Cretaceous. *Annals of the Missouri Botanical Garden*, *86*(2), 373–406. https://doi.org/10.2307/2666181

Grocke, D. R. (2002). The carbon isotope composition of ancient CO_2 based on higher-plant organic matter. *Philosophical Transactions of the Royal Society of London. Series A: Mathematical, Physical and Engineering Sciences*, *360*(1793), 633–658. https://doi.org/10.1098/rsta.2001.0965

Harper, D. T., Hönisch, B., Zeebe, R. E., Shaffer, G., Haynes, L. L., Thomas, E., & Zachos, J. C. (2020). The Magnitude of Surface Ocean Acidification and Carbon Release During Eocene Thermal Maximum 2 (ETM-2) and the Paleocene-Eocene Thermal Maximum (PETM). *Paleoceanography and Paleoclimatology*, *35*(2). https://doi.org/10.1029/2019PA003699

Harrell Jr, T. L., Pérez-Huerta, A., & Suarez, C. A. (2016). Endothermic mosasaurs? Possible thermoregulation of Late Cretaceous mosasaurs (Reptilia, Squamata) indicated by stable oxygen isotopes in fossil bioapatite in comparison with coeval marine fish and pelagic seabirds. *Palaeontology*, *59*(3), 351–363. https://doi.org/10.1111/pala.12240

Herriott, T. M., Crowley, J. L., Schmitz, M. D., Wartes, M. A., & Gillis, R. J. (2019). Exploring the law of detrital zircon: LA-ICP-MS and CA-TIMS geochronology of Jurassic forearc strata, Cook Inlet, Alaska, USA. *Geology*, *47*(11), 1044–1048. https://doi.org/10.1130/G46312.1

Herrle, J. O., Schröder-Adams, C. J., Davis, W., Pugh, A. T., Galloway, J. M., & Fath, J. (2015). Mid-Cretaceous High Arctic stratigraphy, climate, and Oceanic Anoxic Events. *Geology*, *43*(5), 403–406. https://doi.org/10.1130/G36439.1

Herrmann, M., Söderlund, U., Scherstén, A., Næraa, T., Holm-Alwmark, S., & Alwmark, C. (2021). The effect of low-temperature annealing on discordance of U–Pb zircon ages. *Scientific Reports*, *11*(1), Article 1. https://doi.org/10.1038/s41598-021-86449-y

Hesselbo, S., Gröcke, D., Jenkyns, H., Bjerrum, C., Farrimond, P., Bell, H., & Green, O. (2000). Massive dissociation of gas hydrate during a Jurassic oceanic anoxic event. *Nature*, *406*, 392–395. https://doi.org/10.1038/35019044

Hochuli, P. A., Menegatti, A. P., Weissert, H., Riva, A., Erba, E., & Silva, I. P. (1999). Episodes of high productivity and cooling in the early Aptian Alpine Tethys. *Geology*, *27*(7), 657. https://doi.org/10.1130/0091-7613(1999)027<0657:EOHPAC>2.3.CO;2

Hong, S. K., & Lee, Y. I. (2012). Evaluation of atmospheric carbon dioxide concentrations during the Cretaceous. *Earth and Planetary Science Letters*, *327–328*, 23–28. https://doi.org/10.1016/j.epsl.2012.01.014

Jahren, A. H., Arens, N. C., Sarmiento, G., Guerrero, J., & Amundson, R. (2001). Terrestrial record of methane hydrate dissociation in the Early Cretaceous. *Geology*, *29*(2), 159. https://doi.org/10.1130/0091-7613(2001)029<0159:TROMHD>2.0.CO;2

Knowlton, F. H. (1916). Note on a recent discovery of fossil plants in the Morrison Formation. *Journal of the Washington Academy of Sciences*, *6*(7), 180–181.

Kump, L. R., & Arthur, M. A. (1999). Interpreting carbon-isotope excursions: Carbonates and organic matter. *Chemical Geology*, *161*(1–3), 181–198.

Leckie, R. M., Bralower, T. J., & Cashman, R. (2002). Oceanic anoxic events and plankton evolution: Biotic response to tectonic forcing during the mid-Cretaceous. *Paleoceanography*, *17*(3), 13-1-13–29. https://doi.org/10.1029/2001PA000623

Lee, C.-T. A., Jiang, H., Dasgupta, R., & Torres, M. (2019). A Framework for Understanding Whole-Earth Carbon Cycling. In B. N. Orcutt, I. Daniel, & R. Dasgupta (Eds.), *Deep Carbon* (1st ed., pp. 313–357). Cambridge University Press. https://doi.org/10.1017/9781108677950.011

Li, X., Jenkyns, H. C., Zhang, C., Wang, Y., Liu, L., & Cao, K. (2014). Carbon isotope signatures of pedogenic carbonates from SE China: Rapid atmospheric pCO2 changes during middle–late Early Cretaceous time. *Geological Magazine*, *151*(5), 830–849. https://doi.org/10.1017/S0016756813000897

Lloyd, G. T., Davis, K. E., Pisani, D., Tarver, J. E., Ruta, M., Sakamoto, M., Hone, D. W. E., Jennings, R., & Benton, M. J. (2008). Dinosaurs and the Cretaceous Terrestrial Revolution. *Proceedings of the Royal Society B: Biological Sciences*, *275*(1650), 2483–2490. https://doi.org/10.1098/rspb.2008.0715

Ludvigson, G. A., Joeckel, R. M., Murphy, L. R., Stockli, D. F., González, L. A., Suarez, C. A., Kirkland, J. I., & Al-Suwaidi, A. (2015). The emerging terrestrial record of Aptian-Albian global change. *Cretaceous Research*, *56*, 1–24. https://doi.org/10.1016/j.cretres.2014.11.008

Lynn, W., & Williams, D. (1992). The Making of a Vertisol. *Soil Survey Horizons*, *33*(2), 45–50. https://doi.org/10.2136/sh1992.2.0045

Mantzios, C. (1986). *The paleosols of the Upper Jurassic Morrison and Lower Cretaceous Cloverly formations, Northeast Bighorn Basin, Wyoming*.

Martin, J. E. (2002). Juvenile marine reptiles from the Late Cretaceous of the Antarctic Peninsula and their relationships to other such occurrences in Central South Dakota And Belgium. *Proceedings of the South Dakota Academy of Science*, *81*.

Maynard, J. B. (1992). Chemistry of Modern Soils as a Guide to Interpreting Precambrian Paleosols. *The Journal of Geology*, *100*(3), 279–289. https://doi.org/10.1086/629632

McAnena, A., Flögel, S., Hofmann, P., Herrle, J. O., Griesand, A., Pross, J., Talbot, H. M., Rethemeyer, J., Wallmann, K., & Wagner, T. (2013). Atlantic cooling associated with a marine biotic crisis during the mid-Cretaceous period. *Nature Geoscience*, *6*(7), 558–561. https://doi.org/10.1038/ngeo1850

McInerney, F. A., & Wing, S. L. (2011). The Paleocene-Eocene Thermal Maximum: A Perturbation of Carbon Cycle, Climate, and Biosphere with Implications for the Future. *Annual Review of Earth and Planetary Sciences*, *39*(1), 489–516. https://doi.org/10.1146/annurev-earth-040610-133431

Moberly, R., JR. (1960). Morrison, Cloverly, and Sykes Mountain Formations, Northern Bighorn Basin, Wyoming and Montana. *GSA Bulletin*, *71*(8), 1137–1176. https://doi.org/10.1130/0016-7606(1960)71[1137:MCASMF]2.0.CO;2

Montañez, I. P. (2013). Modern soil system constraints on reconstructing deep-time atmospheric CO2. *Geochimica et Cosmochimica Acta*, *101*, 57–75. https://doi.org/10.1016/j.gca.2012.10.012

Nolan, C. E. (2000). Fluvial hydraulics, geometries, migration, and associated alluvial architecture of the Lower Cretaceous Cloverly Formation, Bighorn Basin, Wyoming. *Bighorn Basin, Wyoming: Unpublished MS Thesis, Indiana University*.

Nordt, L. C., & Driese, S. D. (2010). New weathering index improves paleorainfall estimates from Vertisols. *Geology*, *38*(5), 407–410. https://doi.org/10.1130/G30689.1

Nudds, J. R., Lomax, D. R., & Tennant, J. P. (2022). Gastroliths and Deinonychus teeth associated with a skeleton of Tenontosaurus from the Cloverly Formation (Lower Cretaceous), Montana, USA. *Cretaceous Research*, *140*, 105327. https://doi.org/10.1016/j.cretres.2022.105327

Oreska, M. P. J., Carrano, M. T., & Dzikiewicz, K. M. (2013). Vertebrate Paleontology of the Cloverly Formation (lower Cretaceous), I: Faunal Composition, Biogeographic Relationships, and Sampling. *Journal of Vertebrate Paleontology*, *33*(2), 264–292.

Ostrom, J. H. (1970). *Stratigraphy and Paleontology of the Cloverly Formation (Lower Cretaceous) of the Bighorn Basin Area, Wyoming and Montana*. Yale University Press.

Porter, A. S., Yiotis, C., Montañez, I. P., & McElwain, J. C. (2017). Evolutionary differences in Δ13C detected between spore and seed bearing plants following exposure to a range of atmospheric O2:CO2 ratios; implications for paleoatmosphere reconstruction.

Geochimica et Cosmochimica Acta, *213*, 517–533. https://doi.org/10.1016/j.gca.2017.07.007

Quadt, A. von, Gallhofer, D., Guillong, M., Peytcheva, I., Waelle, M., & Sakata, S. (2014). U–Pb dating of CA/non-CA treated zircons obtained by LA-ICP-MS and CA-TIMS techniques: Impact for their geological interpretation. *Journal of Analytical Atomic Spectrometry*, *29*(9), 1618–1629. https://doi.org/10.1039/C4JA00102H

Röhl, U., Westerhold, T., Bralower, T. J., & Zachos, J. C. (2007). On the duration of the Paleocene-Eocene thermal maximum (PETM). *Geochemistry, Geophysics, Geosystems*, *8*(12). https://doi.org/10.1029/2007GC001784

Saltzman, M. R., & Thomas, E. (2012). Carbon Isotope Stratigraphy. In *The Geologic Time Scale* (pp. 207–232). Elsevier. https://doi.org/10.1016/B978-0-444-59425-9.00011-1

Schoene, B., Samperton, K. M., Eddy, M. P., Keller, G., Adatte, T., Bowring, S. A., Khadri, S. F. R., & Gertsch, B. (2015). U-Pb geochronology of the Deccan Traps and relation to the end-Cretaceous mass extinction. *Science*, *347*(6218), 182–184. https://doi.org/10.1126/science.aaa0118

Sheldon, N. D., Retallack, G. J., & Tanaka, S. (2002). Geochemical Climofunctions from North American Soils and Application to Paleosols across the Eocene-Oligocene Boundary in Oregon. *The Journal of Geology*, *110*(6), 687–696. https://doi.org/10.1086/342865

Shurr, G. W., Anna, L. O., & Peterson, J. A. (1989). Zuni Sequence in Williston Basin—Evidence for Mesozoic Paleotectonism1. *AAPG Bulletin*, *73*(1), 68–87. https://doi.org/10.1306/703C9AEB-1707-11D7-8645000102C1865D

Suarez, C. A., Knobbe, T. K., Crowley, J. L., Kirkland, J. I., & Milner, A. R. C. (2017). A chronostratigraphic assessment of the Moenave Formation, USA using C-isotope

chemostratigraphy and detrital zircon geochronology: Implications for the terrestrial end Triassic extinction. *Earth and Planetary Science Letters*, *475*, 83–93. https://doi.org/10.1016/j.epsl.2017.07.028

Suarez, M. B., Ludvigson, G. A., González, L. A., Al-Suwaidi, A. H., & You, H.-L. (2013). Stable isotope chemostratigraphy in lacustrine strata of the Xiagou Formation, Gansu Province, NW China. *Geological Society, London, Special Publications*, *382*(1), 143–155.

Sundquist, E., & Visser, K. (2003). *The Geologic History of the Carbon Cycle: Treatise on Geochemistry*. doi:10.1016/B0-08-043751-6/08133-0.

Timm, C., Hoernle, K., Werner, R., Hauff, F., Den Bogaard, P. V., Michael, P., Coffin, M. F., & Koppers, A. (2011). Age and geochemistry of the oceanic Manihiki Plateau, SW Pacific: New evidence for a plume origin. *Earth and Planetary Science Letters*, *304*(1–2), 135–146. https://doi.org/10.1016/j.epsl.2011.01.025

Trujillo, K., & Kowallis, B. (2015). Recalibrated legacy 40Ar/39Ar ages for the Upper Jurassic Morrison Formation, Western Interior, U.S.A. *Geology of the Intermountain West*, *2*, 1–8. https://doi.org/10.31711/giw.v2.pp1-8

Vuke-Foster, S. M. (1982). *Depositional environments of the Cretaceous Thermopolis Muddy and Mowry Formations southern Madison and Gallatin Ranges Montana*.

Way, J. N., O'Malley, P. J., Suttner, L. J., & Furer, L. C. (1998). *Tectonic controls on alluvial systems in a distal foreland basin: The Lakota and Cloverly formations (Early Cretaceous) in Wyoming, Montana and South Dakota*.

Weissert, H., Lini, A., Föllmi, K. B., & Kuhn, O. (1998). Correlation of Early Cretaceous carbon isotope stratigraphy and platform drowning events: A possible link? *Palaeogeography,*

Palaeoclimatology, Palaeoecology, *137*(3), 189–203. https://doi.org/10.1016/S0031-0182(97)00109-0

White, W. M. (2014). *Isotope Geochemistry*. John Wiley & Sons.

Wieland, G. R. (1905). Notes on the stratigraphy and paleontology of the Black Hills rim. *Status of the Mesozoic Flora of the United States: Second Paper. Washington, DC: United States Government Printing Office*, 317–326.

Wignall, P. B. (2001). Large igneous provinces and mass extinctions. *Earth-Science Reviews*, *53*(1), 1–33. https://doi.org/10.1016/S0012-8252(00)00037-4

Wignall, P. B. (2005). The Link between Large Igneous Province Eruptions and Mass Extinctions. *Elements*, *1*(5), 293–297. https://doi.org/10.2113/gselements.1.5.293

Zachos, J. C., Röhl, U., Schellenberg, S. A., Sluijs, A., Hodell, D. A., Kelly, D. C., Thomas, E., Nicolo, M., Raffi, I., Lourens, L. J., McCarren, H., & Kroon, D. (2005). Rapid Acidification of the Ocean During the Paleocene-Eocene Thermal Maximum. *Science*, *308*(5728), 1611–1615. https://doi.org/10.1126/science.1109004

Zaleha, M. J. (2006). Sevier orogenesis and nonmarine basin filling: Implications of new stratigraphic correlations of Lower Cretaceous strata throughout Wyoming, USA. *Geological Society of America Bulletin*, *118*(7–8), 886–896. https://doi.org/10.1130/B25715.1

Zaleha, M. J., & Wiesemann, S. A. (2005). Hyperconcentrated Flows and Gastroliths: Sedimentology of Diamictites and Wackes of the Upper Cloverly Formation, Lower Cretaceous, Wyoming, U.S.A. *Journal of Sedimentary Research*, *75*(1), 43–54. https://doi.org/10.2110/jsr.2005.005

Zeebe, R. E., Zachos, J. C., & Dickens, G. R. (2009). Carbon dioxide forcing alone insufficient to explain Palaeocene–Eocene Thermal Maximum warming. *Nature Geoscience*, *2*(8), 576–580. https://doi.org/10.1038/ngeo578

Zi, J.-W., Rasmussen, B., Muhling, J. R., & Fletcher, I. R. (2022). In situ U-Pb and geochemical evidence for ancient Pb-loss during hydrothermal alteration producing apparent young concordant zircon dates in older tuffs. *Geochimica et Cosmochimica Acta*, *320*, 324–338. https://doi.org/10.1016/j.gca.2021.11.038

Appendix A: Cloverly formation field notes at the Crooked Creek section and $\delta^{13}C_{org}$ isotopic composition

Thickness	Cumulative Thickness (m)	$\delta^{13}C_{org}$ VPDB	Total Organic Carbon (TOC) %	Lithologic Description
CCC-01	3	-23.38	0.06	Very fine sandstone with charcoal bits
CCC-02	4.5	-24.56	0.04	Fine to medium sized oxidized grains
CCC-03	6.5	-24.66	0.04	Very fine to fine sa7ndstone with some black bits present
CCC-04	10.5	-21.67	0.12	Dark gray silty mudstone
CCC-05	12	-22.63	0.11	Gray muddy sand
CCC-06	12.25	-23.00	0.11	Gray muddy sand Gray muddy fine to very fine sand- sample getting muddy
CCC-07	12.50	-23.63	0.09	Light gray silty mudstone
CCC-08	13.75	-21.79	0.14	Dark gray silty mudstone
CCC-09	14	-22.00	0.10	Light gray silty mudstone
CCC-10	15	-22.88	0.20	Dark gray mudstone
CCC-11	14.75	-23.39	0.07	Tan Mudstone
CCC-12	14.50	-22.06	0.15	Gray mudstone with lots of ostracods
CCC-13	15.10	-21.31	0.08	Dark gray mudstone
CCC-14	15.60	-21.43	0.11	Dark gray mudstone
CCC-15	16.00	-24.22	0.21	Very light gray limestone with slickensides. Organic???
CCC-16	16.25	-23.92	0.22	Same as below
CCC-17	16.50	-23.25	0.06	Gray mudstone with pea-sized carbonate nodules and slickensides. Ostracods present
CCC-18	16.75	-23.70	0.05	Dark gray mudstone with slickensides and carbonate nodules present
CCC-19	17.00	-23.61	0.06	Same as below
CCC-20	17.25	-22.00	0.19	Same as below but no nodules
CCC-21	17.50	-21.79	0.19	Has some bits
CCC-22	17.75	-22.65	0.12	Dark gray mudstone with large slickensides
CCC-23	18.00	-23.06	0.09	Gray mudstone with carbonate nodules and white mottles. Roots??
CCC-24	18.25	-25.13	0.09	Dark gray mudstone with very shiny slickensides and large carbonate
CCC-25	18.50	-23.12	0.08	Same as below
CCC-26	18.75	-23.30	0.09	Grayish purple mudstone
CCC-27	19.00	23.03	0.13	Very dark gray mudstone with slickensides
CCC-28	19.25	-23.21	0.19	Same as below
CCC-29	19.50	-23.82	0.09	Same as below with larger slickensides
CCC-30	19.75	-24.93	0.09	Lighter gray mudstone with slickensides
CCC-31	20.00	-26.41	0.05	Grayish green mudstone with orange mottles and slickensides
CCC-32	20.25	-22.90	0.5	Dark gray mudstone
CCC-33	20.50	-22.98	0.4	Same as below
CCC-34	20.75	-22.89	0.3	Same as below
CCC-35	21.00	-22.83	0.3	Mudstone
CCC-36	24.25	-22.65	0.21	Dark gray mudstone
CCC-37	24.50	-22.75	0.19	Same as below
CCC-38	24.75	-22.67	0.16	Same as below
CCC-39	25.00	-22.49	0.24	Same as below with slickensides
CCC-40	25.25	-23.48	0.13	Same as below with slickensides
CCC-41	25.50	-23.89	0.09	Gray mudstone with slickensides
CCC-42	25.75	-22.95	0.08	Gray greenish mudstone
CCC-43	26.00	-23.02	0.08	Same as below with clear slickensides
CCC-44	26.25	-23.65	0.07	Mud-gray claystone

CCC-45	26.50	-25.11	0.16	Mud-gray claystone with root trace and faint green mottles
CCC-46	26.75	-24.64	0.12	Mud-gray claystone with black fragments
CCC-47	27.00	-23.42	0.51	Gray mud with some black organic fragments
CCC-48	28.00	-22.87	0.36	Cover
CCC-49	28.25	-22.97	0.09	Gray mudstone with some slickensides
CCC-50	28.50	-23.44	0.07	Gray clay/mudstone
CCC-51	29.50	-24.54	0.10	Gray and brick red siltstone with green mottles
CCC-52	29.5	-24.23	0.07	Dark red muddy siltstone with grayish green mottles and slickensides
CCC-53	30.00	-23.82	0.10	Same as below
CCC-54	30.25	-24.15	0.07	Same as below
CCC-55	30.75	-25.46	0.07	Red and green noduled muddy siltstone with slickensides
CCC-56	31.00	-23.59	0.04	Red siltstone with fine green mottles and larger purple nodules
CCC-57	31.25	-26.08	0.05	Red muddy siltstone with fine green mottles and slickensides
CCC-58	31.50	-23.63	005	Red and purplish gray muddy siltstone/silty mudstone with tapering root trace
CCC-59	31.75	-24.10	0.03	Dark gray silty mudstone with green mottles and slickensides
CCC-60	32.00	-24.73	0.03	Same as below but more reddish with some greenish mottles and yellowy orange mottles
CCC-61	32.25	-26.51	0.02	Has some ripples in sand with mud fragments and tarnish green ripples
CCC-62	32.50	-25.53	0.03	Same as below
CCC-63	32.75	-26.05	0.02	Same as below but poorly sorted quartz
CCC-64	33.00	-25.87	0.04	Same as below but no ripples
CCC-65	33.50	-27.48	0.04	Reddish sand
CCC-66	34.00	-25.91	0.03	Same as below
CCC-67	35.30	-26.54	0.02	Top of sand
CCC-68	35.55	-25.35	0.04	Green fine sandstone with purple mottles and black bits. Base of quarry
CCC-69	35.80	-24.18	0.06	Same as below. Himes
CCC-70	36.05	-24.20	0.07	Same as below
CCC-71	36.30	-24.66	0.13	Very fine green sandstone with purple and orange mottles
CCC-72	36.55	-23.32	0.08	More purple siltstone with green and yellow mottles. Fish tooth present ??
CCC-73	36.80	-24.61	0.04	Purplish red siltstone with green and orange mottles
CCC-74	37.05	-23.94	0.11	Very fine clear purplish red fine to gray siltstone with green and orange mottles. Iron oxide nodules present?
CCC-75	37.30	-24.41	0.07	Purplish red siltstone with green and orange mottles
CCC-76	37.55	-24.68	0.06	Very fine clear purplish red fine to gray siltstone with green and orange mottles. Iron oxide nodules present?
CCC-77	37.50	-23.84	0.08	Green very fine sandstone with purple mottles and black organic bits
CCC-78	38.05	-24.58	0.08	Very fine sandstone to siltstone. Red with light gray mottles plus pea sized to walnut sized carbonate nodule
CCC-79	38.30	-26.02	0.08	Red siltstone with gray mottles, A/B horizon
CCC-80	38.55	-24.85	0.05	Red siltstone with gray mottles, A/B horizon
CCC-81	38.80	-24.92	0.06	Red with purple mottle siltstone with slickensides and carbonate nodule
CCC-82	39.20	-24.39	0.05	Brick red siltstone with slickensides
CCC-83	39.45	-24.71	0.05	Brick red siltstone with slickensides
CCC-84	39.70	-25.16	0.05	Brick red siltstone with slickensides and gray mottles
CCC-85	39.95	-24.81	0.06	Brick red siltstone with slickensides and gray mottles
CCC-86	40.20	-24.14	0.05	Brick red siltstone with slickensides
CCC-87	40.45	-23.63	0.05	Brick red siltstone with slickensides
CCC-88	40.70	-25.97	0.06	Brick red siltstone with fine mottles

CCC-89	40.95	-22.24	0.06	Brick red siltstone with slickensides
CCC-90	41.20	-24.60	0.05	Brick red siltstone with slickensides + fine green mottles
CCC-91	41.45	-24.37	0.06	Brick red siltstone with slickensides + fine green mottles
CCC-92	41.70	-24.93	0.06	Brick red siltstone with slickensides + larger green mottles
CCC-93	41.95	-24.29	0.05	Brick red siltstone with slickensides
CCC-94	42.20	-25.21	0.08	Brick red siltstone with green mottles + slickensides
CCC-95	42.45	-24.43	0.05	Brick red siltstone with slickensides
CCC-96	42.70	-24.07	0.07	Yellow fine sandstone. Approximately 5cm thick
CCC-97	42.95	-24.73	0.05	Yellow fine sandstone. Approximately 5cm thick
CCC-98	43.20	-24.56	0.05	Brick red siltstone with green mottles + slickensides
CCC-99	43.45	-21.96	0.05	Brick red siltstone with purple mottles + orange mottles + slickensides
CCC-100	43.70	-23.27	0.05	Brick red siltstone with orange mottles
CCC-101	43.95	-24.31	0.05	Brick red siltstone with orange mottles + purple mottles with slickensides
CCC-102	44.20	-24.44	0.05	Brick red siltstone with orange mottles + purple mottles with slickensides
CCC-103	44.45	-24.27	0.03	Purple +gray siltstone with orange mottles + Fe-oxide nodules
CCC-104	44.70	-24.15	0.04	Green + purple muddy siltstone with orange mottles + slickensides
CCC-105	44.95	-24.84	0.05	Purple + grayish blue muddy siltstone with orange mottles + slickensides
CCC-106	45.20	-24.36	0.03	Purple + grayish blue muddy siltstone with orange mottles + slickensides
CCC-107	45.45	-30.20	0.08	Purple + grayish blue muddy siltstone with orange mottles + slickensides+ root mottles ??
CCC-108	45.70	-23.93	0.04	Gray/purple siltstone
CCC-109	45.95	-24.87	0.03	Gray/purple siltstone with metal oxide nodules
CCC-110	46.20	-22.96	0.04	Gray + purple siltstone with slickensides + orange mottles
CCC-111	46.45	-23.43	0.09	Gray silty mudstone with floating FSS - sized pebbles + organic bits
CCC-112	46.70	-23.37	0.10	Gray silty mudstone + orange mottles
CCC-113	47.00	-23.42	0..18	Gray siltstone
CCC-114	47.25	-23.35	0.19	Gray siltstone with root mottles
CCC-115	47.50	-23.46	0.14	Gray silty mudstone with slickensides
CCC-116	47.75	-22.83	0.16	Gray + brick red with muddy orange root mottles siltstone
CCC-117	48.15	-23.44	0.05	Light gray silty mudstone
CCC-118	48.55	-23.51	0.06	Light gray silty mudstone with fine orange root mottles
CCC-119	48.95	-23.87	0.09	Fe-oxide nodules ???
CCC-120	49.15	-23.93	0.17	Gray muddy siltstone with slickensides
CCC-121	49.50	-22.73	0.21	Gray with very large purple mottles with lots of fine orange mottles
CCC-122	49.85	-23.14	0.14	Gray silty mudstone
CCC-123	50.20	-23.36	0.27	Same as CCC-122
CCC-124	50.55	-23.07	0.18	Same as CCC-123
CCC-125	50.95	-23.61	0.24	Same as CCC- 123 + organic bits
CCC-126	51.20	-24.64	0.25	Same as CCC-125 but shaley
CCC-127	51.55	-24.71	0.14	Same as CCC-126
CCC-128	51.8	-24.53	0.16	Same as CCC-127, probably same level as charcoal sample
CCC-129	52.05	-22.76	0.09	Mottled red + gray siltstone
CCC-130	52.30	-22.68	0.18	Gray siltstone
CCC-131	53.80	-23.10	0.19	Gray siltstone
CCC-132	54.05	-23.42	0.13	Greenish grey siltstone
CCC-133	54.30	-23.44	0.03	Greenish grey siltstone with red mottles
CCC-134	54.55	-23.47	0.04	Very fine sandstone - light greenish gray + yellow. Both sandstone + gray mud sampled
CCC-135	54.80	-24.32	0.04	Gray with red root mottles, very fine sandstone
CCC-136	55.05	-23.61	0.04	Light grey very fine sandstone with yellow mottles + red fine root

				traces
CCC-137	55.30	-24.36	0.08	Yellowish gray muddy very fine sandstone with purple mottles
CCC-138	55.55	-25.20	0.03	Light gray very fine sandstone with orange mottles
CCC-139	55.80	-24.74	0.03	Tan fine sandstone with muddy root mottles
CCC-140	56.05	-25.12	0.02	Tan fine sandstone with black staining
CCC-141	56.30	-24.71	0.04	Gray fine sandstone with orange mottles above a grey silt with large red root mottles
CCC-142	56.55	-25.91	0.04	Gray very fine sandstone with orange-red root mottles
CCC-143	56.80	-24.17	0.07	Gray siltstone with large -Fe oxide nodules?
CCC-144	57.05	-24.02	0.03	Gray very fine sandstone with orange fine root mottles
CCC-145	57.30	-24.74	0.06	Gray very fine sandstone with orange mottles. Also sampled the mudstone above
CCC-146	57.55	-25.03	0.07	Greenish/yellow grey muddy siltstone
CCC-147	58.80	-24.00	0.06	Greenish/yellow gray muddy siltstone
CCC-148	58.05	-24.74	0.05	Brown muddy siltstone
CCC-149	58.30	-25.03	0.04	Same as 148
CCC-150	58.55	-24.00	0.08	Gray silty mudstone with some large red mottles + fine orange root mottles
CCC-151	58.80	-23.90	0.05	Orange/tan siltstone
CCC-152	59.05	-24.34	0.09	Gray/orange skinned muddy siltstone
CCC-153	59.30	-23.31	0.14	Gray + yellow stained muddy siltstone with Fe-oxide-stained resistive layers
CCC-154	59.55	-23.77	0.64	Gray silty shale
CCC-155	60.05	-23.51	0.45	Gray silty shale with interbedded resistant with Fe-Oxide cemented layers
CCC-156	60.30	-23.62	0.65	Same as 155
CCC-157	60.55	-23.69	0.41	Grey silty mudstone + shale with interbedded Fe-Oxide cement units. Some plant fragments + charcoal
CCC-158	60.80	-23.14	0.58	Same as 157
CCC-159	61.05	-23.79	0.17	Grey silty mudstone with yellow staining + lots of plant fragments
CCC-160	61.30	-23.95	0.07	Gray shale (paper thin) with interbedded Fe-oxide cemented layers with plant fragments. Organic bits in grey shale too
CCC-161	61.55	-23.42	0.23	Gray shale (paper thin) with interbedded Fe-oxide cemented layers with plant fragments. Organic bits in grey shale too
CCC-162	61.80	-23.41	0.57	Same as 161
CCC-163	62.05	-23.18	0.20	Bright yellow very fine sandstone/fine sandstone with interbedded fissile grey shale with plant fern samples
CCC-164	63.00	-28.84	0.06	Tan quartzarenite mud sandstone. Top of Sykes Mountain